Micromechanical analysis of porous SMA

V Sepe[1], F Auricchio[2], S Marfia[1] and E Sacco[1]

[1] University of Cassino and Southern Lazio, Italy
[2] University of Pavia, Italy

E-mail: v.sepe@unicas.it, auricchio@unipv.it, marfia@unicas.it and sacco@unicas.it

CrossMark

Abstract

The present paper deals with computational micromechanical analyses of porous shape memory alloy (SMA). Porous SMAs are considered composite materials made of a dense SMA matrix including voids. A three-dimensional constitutive law is presented for the dense SMA able to reproduce the pseudo-elastic as well as the shape memory effects and, moreover, to account for the different elastic properties of the austenite and martensite phases. Furthermore, a numerical procedure is developed and the overall behavior of the porous SMA is recovered studying a representative volume element. Comparisons between the numerical results, recovered using the proposed modeling, and experimental data available in the literature are presented. The case of closed and open porosity is investigated. Parametric studies have been conducted in order to investigate the influence of the porosity, the shape and orientation of the pores on the overall mechanical response and, mainly, on the energy absorption dissipation capability.

Keywords: porous material, shape memory alloys, micromechanics, energy dissipation

(Some figures may appear in colour only in the online journal)

1. Introduction

Porous shape memory alloys (SMAs) are materials obtained by sintering nickel and titanium powders. They can be considered active composites characterized by the presence of pores of different shape, size and orientation in a SMA matrix. Manufacturing and testing of these materials have been performed initially by Martynova *et al* [1] and Li *et al* [2], while fabrication techniques have been investigated by Vandygriff *et al* [3]. Many efforts have been expended in the last few years to develop manufacturing processes able to achieve microstructures characterized by high porosity, regular pore shape and distribution in relation with the resulting mechanical and transformation behavior.

Porous SMAs combine the benefit of the smart response, such as pseudo-elastic and shape memory effects, with the properties of porous or foamed metals, such as low density, high surface area and high permeability. In fact, they present good mechanical properties, good corrosion resistance, high biocompatibility and high dissipation capacity, that make them attractive for the development of several innovative applications, like human body implants, light-weight actuators and energy absorption devices.

In particular, porous NiTi are very promising materials for biomedical applications mainly for the development of orthopedic implants, as they allow ingrowth of osteoblasts and tissues, promoting long-term fixation of bone implants; moreover, they are characterized by low Young's modulus and by a pseudo-elastic behavior similar to bone and tendons [4–6]. A quite current review concerning the manufacturing and the use of porous SMAs for biomedical applications is presented in [7].

On the other hand, porous NiTi is characterized by density lower than NiTi with high energy absorption capability per volume unit. This makes porous NiTi a good candidate as energy absorbing material in various fields of applications [8].

Different approaches have been used for modeling the response of porous SMA. Among the others Ashrafi *et al* [9] and Ashrafi *et al* [10] proposed a thermodynamically consistent model for dense and porous SMA able to account for the porosity density in the pseudoelastic and shape memory response.

One of the most active research approaches involves the micromechanical analysis and the homogenization technique. In fact, overall constitutive laws of porous SMAs have been
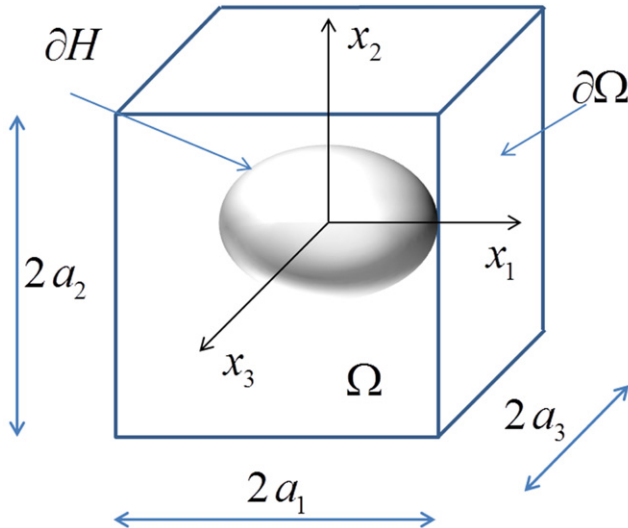
Figure 1. Porous NiTi SMA periodic unit cell.

deduced studying the response of unit cells (UCs) presenting open or closed pores characterized by a circular cross section; micromechanical analyses have been developed using the finite element approach or the incremental Mori–Tanaka averaging scheme [11]. Mori–Tanaka and self-consistent methods have been used as averaging schemes for the prediction of the macroscopic response of porous SMAs [12–15]. In particular, Nemat-Nasser *et al* [16] developed an experimental study with a micromechanical analysis based on the Mori–Tanaka approach, modeling the porous SMA as a three phase composite.

Qidwai and De Giorgi [17] implemented computational mesomechanical techniques to estimate the response of porous SMAs in the framework of a two-dimensional finite element, considering randomly distributed pores. Then, they developed finite element simulations of a split Hopkinson bar test made of a hybrid SMA composite obtained by filling the pores of a porous SMA matrix with a polymeric material [18].

Panico and Brinson [19] developed a micromechanical finite element analysis of a porous SMA representative volume element (RVE), characterized by a random void distribution, in order to study the complex interaction between porosity, local phase transformation and macroscale response. Liu *et al* [20] investigated the effect of the hydrostatic stress on the overall behavior of porous SMA, considering the porous SMA as an assembly of composite spheres of various sizes. Recently, a micromechanical study of porous SMA using the finite element approach has been presented in [21].

As the porous SMA can be successfully adopted in several appealing and advanced applications, the need of further studies on the modeling of this smart material is growing in order to capture the specific features of the mechanical behavior with a particular attention on the energy dissipation capability.

On the basis of the recent enhancement in the manufacturing process aimed at producing porous SMAs with regular pore shape, orientation and distribution, the need of better understanding how these factors influence the mechanical response arises. In fact, the improvement in the manufacturing process could allow for designing the material addressed to a specific application.

To fulfill this need, the aim of the present paper is the development of a micromechanical analysis of porous SMA, considering the presence of voids of different size, shape and orientation inside a NiTi dense matrix, in order to understand the influence of these factors on the overall behavior of the material. In other words, the problem of the derivation of a constitutive model for the porous SMA material using the methods of the micromechanics and homogenization is approached. The constitutive law of porous SMAs is established considering a suitable RVE, where the mechanical properties of the dense SMA and information about pore geometry are given. A constitutive model able to reproduce the pseudo-elastic as well as the shape memory effects is considered for the dense SMA, based on the model proposed in [22–24]. The SMA model is enhanced considering different elastic properties for the austenite and martensite phases [25] and it is formulated in the framework of small strain.

A numerical procedure is developed and implemented in the finite element code FEAP [26]. Numerical applications are carried out to assess the ability of the proposed model to successfully reproduce the mechanical response and to investigate the energy absorption capability of porous SMAs. Moreover, comparisons with experimental results, available in the literature, are performed. The case of closed or open pore is investigated, studying the effect of the shape of the pore on the response of the material. In particular, numerical analyses are performed prescribing the average strain components.

The main novelty of the present study, with respect to the available literature, is the evaluation of the energy absorption capability of the porous SMAs as function of the geometrical characteristics of the pores, taking into account:

- the use of a SMA constitutive model which considers different elastic moduli of the austenite and the martensite phases;
- the development of systematic parametric analyses in the response of porous SMAs considering different size, shape and orientation of open or closed pores.

In the following the model is described adopting the Voigt notation, i.e. second order tensors are represented as vectors and fourth order tensors as matrices. In particular, the strains and the stresses are reported as vectors with six components, while a symmetric 6×6 matrix defines the elastic constitutive matrix.

The paper is organized as follows. In section 2, the micromechanical formulation for the porous SMA RVE is illustrated; in section 3, the constitutive model of the dense SMA material is presented; numerical applications are given in section 4. Finally, in section 5 concluding remarks are reported.

2. Micromechanical analysis of porous SMA

The constitutive behavior of porous SMA can be derived considering the material as heterogeneous made of a dense SMA matrix and assuming pores as inclusions. The overall response of this very special porous material can be derived using the micromechanical approach and the homogenization technique [11].

In the following, a micromechanical analysis is performed considering a periodic microstructure for the porous SMA made of a dense SMA matrix with the inclusion of voids. Thus, a repetitive UC, denoted as Ω, with a pore H, is illustrated in figure 1 and analyzed prescribing suitable boundary conditions in order to obtain the overall behavior of the whole heterogeneous material. The porosity of the UC is defined as:

$$f = \frac{V_p}{V}, \tag{1}$$

where V_p and V are the volumes of the pore and the whole UC, respectively.

Introducing a Cartesian reference system (O, x_1, x_2, x_3) in the UC, the displacement vector field $\mathbf{u} = \{u_1 \quad u_2 \quad u_3\}^{\mathsf{T}}$ at the typical point $\mathbf{x} = \{x_1 \quad x_2 \quad x_3\}^{\mathsf{T}}$ of Ω is written in the form:

$$\mathbf{u}(\mathbf{x}) = \mathbf{X}^V \bar{\boldsymbol{\varepsilon}} + \tilde{\boldsymbol{u}}(\mathbf{x})$$

$$\text{with} \quad \mathbf{X}^V = \begin{bmatrix} x_1 & 0 & 0 & \frac{1}{2}x_2 & 0 & \frac{1}{2}x_3 \\ 0 & x_2 & 0 & \frac{1}{2}x_1 & \frac{1}{2}x_3 & 0 \\ 0 & 0 & x_3 & 0 & \frac{1}{2}x_2 & \frac{1}{2}x_1 \end{bmatrix}, \tag{2}$$

where $\bar{\boldsymbol{\varepsilon}} = \left\{ \bar{\varepsilon}_{11} \ \bar{\varepsilon}_{22} \ \bar{\varepsilon}_{33} \ \bar{\gamma}_{12} \ \bar{\gamma}_{23} \ \bar{\gamma}_{13} \right\}^{\mathsf{T}}$ is the average total strain and $\tilde{\boldsymbol{u}}(\mathbf{x})$ is the periodic displacement.

The local strain $\boldsymbol{\varepsilon}$ at a typical point $\mathbf{x}$ of Ω is obtained as:

$$\boldsymbol{\varepsilon}(\mathbf{x}) = \bar{\boldsymbol{\varepsilon}} + \tilde{\boldsymbol{\varepsilon}}(\mathbf{x}), \tag{3}$$

with $\tilde{\boldsymbol{\varepsilon}}(\mathbf{x})$ the periodic part of the total strain, characterized by null average in Ω and associated to $\tilde{\boldsymbol{u}}(\mathbf{x})$. For parallelepiped 3D UC with the total dimensions along the coordinate axes x_1, x_2 and x_3 denoted by $2a_1$, $2a_2$ and $2a_3$, the classical periodicity conditions have to be prescribed to the displacement field [27, 28]:

$$\tilde{\boldsymbol{u}}(a_1, x_2, x_3) = \tilde{\boldsymbol{u}}(-a_1, x_2, x_3)$$
$$\forall \ x_2, \ x_3 \ \in [-a_2, a_2] \times [-a_3, a_3],$$
$$\tilde{\boldsymbol{u}}(x_1, a_2, x_3) = \tilde{\boldsymbol{u}}(x_1, -a_2, x_3)$$
$$\forall \ x_1, \ x_3 \ \in [-a_1, a_1] \times [-a_3, a_3],$$
$$\tilde{\boldsymbol{u}}(x_1, x_2, a_3) = \tilde{\boldsymbol{u}}(x_1, x_2, -a_3)$$
$$\forall \ x_1, \ x_2 \ \in [-a_1, a_1] \times [-a_2, a_2]. \tag{4}$$

The SMA matrix stress–strain law, discussed in the next section, allows us to evaluate the local stress $\boldsymbol{\sigma}$ as a function of the strain $\boldsymbol{\varepsilon}$.

The average strain vector $\bar{\boldsymbol{\varepsilon}}$ and the average stress vector $\bar{\boldsymbol{\sigma}}$ are defined in Ω, respectively, as:

$$\bar{\boldsymbol{\varepsilon}} = \frac{1}{V} \int_{\partial\Omega} \mathbf{N}(\mathbf{x})\mathbf{u}(\mathbf{x})\mathrm{d}A$$
$$= \frac{1}{V} \int_{\Omega} \boldsymbol{\varepsilon}(\mathbf{x})\mathrm{d}V - \frac{1}{V} \int_{\partial H} \mathbf{N}(\mathbf{x})\mathbf{u}(\mathbf{x})\mathrm{d}A,$$
$$\bar{\boldsymbol{\sigma}} = \frac{1}{V} \int_{\partial\Omega} \mathbf{X}^S \mathbf{t}(\mathbf{x})\mathrm{d}A$$
$$= \frac{1}{V} \int_{\Omega} \boldsymbol{\sigma}(\mathbf{x})\mathrm{d}V - \frac{1}{V} \int_{\partial H} \mathbf{X}^S \mathbf{t}(\mathbf{x})\mathrm{d}A, \tag{5}$$

with

$$\mathbf{N}(\mathbf{x}) = \begin{bmatrix} n_1 & 0 & 0 \\ 0 & n_2 & 0 \\ 0 & 0 & n_3 \\ n_2 & n_1 & 0 \\ 0 & n_3 & n_2 \\ n_3 & 0 & n_1 \end{bmatrix}, \quad \mathbf{X}^S = \begin{bmatrix} x_1 & 0 & 0 \\ 0 & x_2 & 0 \\ 0 & 0 & x_3 \\ x_2 & x_1 & 0 \\ 0 & x_3 & x_2 \\ x_3 & 0 & x_1 \end{bmatrix}, \tag{6}$$

n_1, n_2 and n_3 being the components of unit vector $\mathbf{n}(\mathbf{x})$ representing the normal to the boundary of the UC $\partial\Omega$. In equation (5), ∂H is the boundary of the void H present in the UC; the traction vector $\mathbf{t}(\mathbf{x})$ is defined as $\mathbf{t} = \mathbf{N}^{\mathsf{T}}\boldsymbol{\sigma}$.

It can be pointed out that the last term in equation (5) is zero since pores are regions with null tractions and it results in $\mathbf{t}(\mathbf{x}) = \mathbf{0}$ at the boundary ∂H.

3. SMA constitutive model

A vast amount of SMA constitutive models are available in the literature. Phenomenological or micromechanical approaches are developed for the definition of satisfactory constitutive laws able to predict the very special response of SMA; the first type of modeling approach has the clear advantage of computational efficiency. Limiting a review to the last five years, among others, Arghavani *et al* [29] proposed a phenomenological constitutive model based on a scalar internal variable, the amount of stress-induced martensite, and on a tensorial internal variable, the preferred direction of variants. The model decouples the pure reorientation mechanism from the pure transformation mechanism. Saleeb *et al* [30] presented a review of the SMA modeling and proposed a thermodynamically consistent model considering the exchange between the stored and dissipated energy. Gu *et al* [31] presented a SMA model based on the use of the martensite volume fraction and the martensite orientation strain tensor; moreover they implemented a numerical procedure into a finite element code. A review of the state-of-the-art in the SMA modeling and application is presented in the recent book [32].

Next, a thermodynamically consistent model, based on the one initially proposed by Souza *et al* [22] and modified first by Auricchio and Petrini [23] and then by Evangelista *et al* [24], is presented in order to describe the mechanical response of the dense SMA material. The model is slightly modified with respect to the one illustrated in [24]: an

improvement to the model is introduced by accounting for different elastic properties of the austenite and single variant martensite phases, which can play a significant role in the overall response of dense and porous SMAs, e.g. [17] and [18]. In fact, experimental evidences demonstrate that the elastic modulus of the martensite phase is lower than the one of the austenite phase (even five times lower). The effect of the variation of the elastic moduli becomes more and more important when approaching the complete phase transformation. In porous SMAs, this occurs also for reduced values of the strain because of the stress concentration around the pores. Hence, it could be very important to take into account the different moduli of the austenite and single variant martensite phases in the evaluation of the mechanical response and in the dissipation of porous SMAs.

The total strain, ε, and the absolute temperature, T, are assumed as control variables while the transformation strain **d**, describing the inelastic strain associated to the austenite–martensite phase transformation, is considered as the internal variable of the model.

The phenomenological model does not distinguish between the SMA phases, austenite and multivariant martensite, as they both correspond to zero transformation strain, i.e. $\mathbf{d} = \mathbf{0}$. Thus, the only phase transformation from austenite or multivariant martensite to single-variant martensite is taken into account.

During the conversion from austenite to single-variant martensite the transformation strain evolves from zero till its norm, $\theta = \| \mathbf{d} \|$, reaches a limit value ε_L, that represents a material parameter, so that the inequality $0 \leqslant \theta \leqslant \varepsilon_L$ has to be satisfied during the phase transformations. The value of ε_L can be determined by a standard uniaxial test.

The free specific energy function is introduced through a convex potential as:

$$\Psi(\varepsilon, \mathbf{d}, T) = \Psi_e(\varepsilon, \mathbf{d}, T) + \Psi_p(\mathbf{d}, T) + \Psi_{\mathrm{id}}(T). \quad (7)$$

The elastic strain energy Ψ_e is a function of the total strain ε, of the inelastic strain **d** and of the absolute temperature T and it results:

$$\Psi_e(\varepsilon, \mathbf{d}, T) = \frac{1}{2}(\varepsilon - \mathbf{d})^{\mathsf{T}}\mathbf{C}(\xi)(\varepsilon - \mathbf{d}), \quad (8)$$

where $\mathbf{C}(\xi)$ is the elasticity constitutive matrix and $\xi = \theta/\varepsilon_L$ represents the volume fraction of the single-variant martensite in a SMA RVE; in particular, when $\xi = 0$ it results $\mathbf{C}(0) = \mathbf{C}^A$ with $\mathbf{C}^A$ the austenite elastic tensor and when $\xi = 1$ it results $\mathbf{C}(1) = \mathbf{C}^S$ with $\mathbf{C}^S$ the single-variant martensite elastic tensor.

The inelastic energy Ψ_p, accounting for all the inelastic phenomena, is related to the internal variable **d** and to the absolute temperature T as:

$$\Psi_p(\mathbf{d}, T) = \beta \left\langle T - M_f \right\rangle \theta + \frac{1}{2}h\theta^2 + \mathscr{I}_{\varepsilon_L}(\theta), \quad (9)$$

with:

- β a material parameter related to the dependence of the transformation stress threshold on the temperature;
- M_f representing the finishing temperature of the austenite–martensite phase transformation evaluated at a stress free state; the symbol $\langle \bullet \rangle$ indicates the positive part of the argument;
- $\theta = ||\mathbf{d}|| = \sqrt{\mathbf{d}^{\mathsf{T}}\mathbf{M}^V\mathbf{d}}$ with

$$\mathbf{M}^V = \begin{bmatrix} \mathbf{I} & \mathbf{0} \\ \mathbf{0} & \frac{1}{2}\mathbf{I} \end{bmatrix}, \quad (10)$$

I and **0** being the 3×3 identity and zero matrices, respectively;

- h a material parameter associated with the slope of the linear stress-transformation strain relation in the uniaxial case;
- $\mathscr{I}_{\varepsilon_L}(\theta)$ the indicator function introduced in order to satisfy the fulfillment of the constraint on the transformation strain norm:

$$\mathscr{I}_{\varepsilon_L}(\theta) = \begin{cases} 0 & \text{if} \quad \theta \leqslant \varepsilon_L \\ +\infty & \text{if} \quad \theta > \varepsilon_L \end{cases}. \quad (11)$$

Equation (11) ensures that the norm of **d** has to be bounded between zero, for the case of a material without oriented martensite, and the maximum value ε_L, for the case of the material fully transformed in single-variant oriented martensite.

The free energy Ψ_{id} is due to the change in temperature with respect to the reference state for an incompressible ideal solid [22–24].

The state laws are derived as:

$$\boldsymbol{\sigma} = \frac{\partial \Psi}{\partial \varepsilon}, \quad (12)$$

$$\mathbf{X} = -\frac{\partial \Psi}{\partial \mathbf{d}}, \quad (13)$$

which define the stress $\boldsymbol{\sigma}$ and the transformation stress **X** as the quantities thermodynamically conjugated to the deformation-like variables ε and **d**, respectively.

Therefore, computing the derivatives in equations (12) and (13), the state laws are:

$$\boldsymbol{\sigma} = \mathbf{C}(\xi)(\varepsilon - \mathbf{d}), \quad (14)$$

$$\mathbf{X} = \boldsymbol{\sigma} - \left[\beta \left\langle T - M_f \right\rangle + h\theta + \gamma \right. \\ \left. - \frac{1}{\varepsilon_L}(\varepsilon - \mathbf{d})^{\mathsf{T}}\frac{\partial \mathbf{C}(\xi)}{\partial \xi}(\varepsilon - \mathbf{d}) \right]\frac{\partial \theta}{\partial \mathbf{d}}, \quad (15)$$

with γ an element of the subdifferential of the indicator function $\mathcal{I}_{\varepsilon_L}(\theta)$ which results as:

$$\gamma \in \partial \mathcal{I}_{\varepsilon_L}(\theta) = \begin{cases} 0 & \text{if } \theta < \varepsilon_L \\ \mathcal{R}^+ & \text{if } \theta = \varepsilon_L. \\ \varnothing & \text{if } \theta > \varepsilon_L \end{cases} \tag{16}$$

The quantity $\boldsymbol{\alpha}$ playing a role similar to the back stress in the classical plasticity theory with kinematic hardening, is defined as:

$$\boldsymbol{\alpha} = \left[\beta \left\langle T - M_f \right\rangle + h\theta + \gamma - \frac{1}{\varepsilon_L} (\boldsymbol{\varepsilon} - \mathbf{d})^{\mathsf{T}} \right. \\ \left. \times \frac{\partial \mathbf{C}(\xi)}{\partial \xi} (\boldsymbol{\varepsilon} - \mathbf{d}) \right] \frac{\partial \theta}{\partial \mathbf{d}}, \tag{17}$$

resulting in a linear function of the temperature when $T > M_f$, thus equation (15) is rewritten in the following form:

$$\mathbf{X} = \boldsymbol{\sigma} - \boldsymbol{\alpha}. \tag{18}$$

Different expressions can be introduced for the elastic matrix $\mathbf{C}(\xi)$; in particular, the alloy can be considered as a composite characterized by the volume fraction ξ of the single-variant martensite in an austenite matrix within a representative volume. The overall elastic response of the composite can be deduced performing a simple homogenization procedure [25]. In particular, the Voigt and Reuss homogenization techniques, leading to well-known overall bounds, are herein considered. Note that the Voigt scheme corresponds to consider the material composed of strips of single variant martensite and austenite parallel to the stress direction. Thus, according to a Voigt homogenization, it results:

$$\mathbf{C}(\xi) = (1 - \xi)\mathbf{C}^A + \xi \mathbf{C}^S, \\ \frac{\partial \mathbf{C}}{\partial \xi} = \mathbf{C}^S - \mathbf{C}^A. \tag{19}$$

According to a Reuss scheme the material is composed of strips of single variant martensite and austenite orthogonal to the stress direction; thus, it results:

$$\mathbf{C}(\xi) = \left[(1 - \xi)\left(\mathbf{C}^A\right)^{-1} + \xi\left(\mathbf{C}^S\right)^{-1} \right]^{-1}, \\ \frac{\partial \mathbf{C}}{\partial \xi} = \left[(1 - \xi)\left(\mathbf{C}^A\right)^{-1} + \xi\left(\mathbf{C}^S\right)^{-1} \right]^{-1} \left[\left(\mathbf{C}^S\right)^{-1} \right. \\ \left. - \left(\mathbf{C}^A\right)^{-1} \right] \left[(1 - \xi)\left(\mathbf{C}^A\right)^{-1} + \xi\left(\mathbf{C}^S\right)^{-1} \right]. \tag{20}$$

In figure 2, the variation of the Young's modulus of the SMA as a function of the single-variant martensite volume
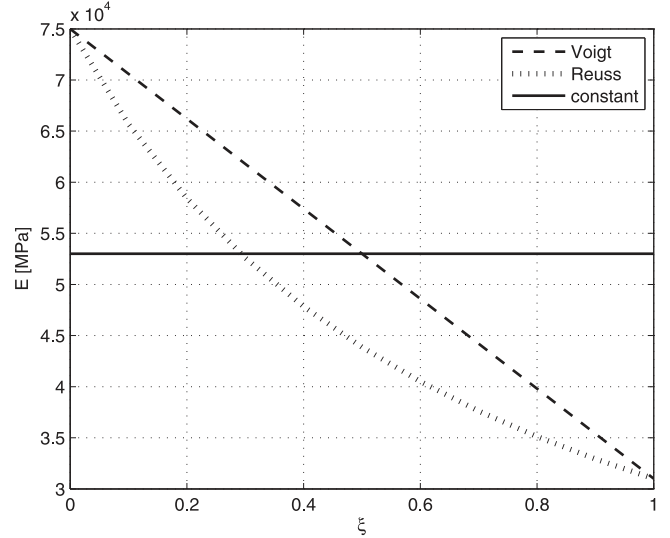

Figure 2. Variation of the effective Young's elastic modulus for the SMA as function of single-variant martensite volume fraction.

fraction is reported for the Voigt and Reuss homogenization schemes in comparison with the average constant value, assuming $E^A = 75\,000$ MPa and $E^S = 31\,000$ MPa. It can be pointed out that the variation of the effective modulus with ξ according to the Voigt scheme is constant. On the contrary, according to the Reuss homogenization the variation, initially, is very fast and, then, becomes slower when ξ tends to 1. This different trend influences the mechanical response of the material.

Among the two homogenization schemes, generally Reuss can be considered more reliable that Voigt, as illustrated in a one-dimensional problem in [25].

The yield function is chosen to depend on the deviatoric part of the thermodynamic force and it is introduced as:

$$F\left(\mathbf{X}^d\right) = \sqrt{2J_2\left(\mathbf{X}^d\right)} - R, \tag{21}$$

where:

- R represents the radius of the elastic domain in the deviatoric space, given by the relation:

$$R = \sqrt{\frac{2}{3}} \sigma_y, \tag{22}$$

  with σ_y the uniaxial critical stress evaluated at $T \leqslant M_f$;
- $\mathbf{X}^d$ is the deviatoric part of the associated variable $\mathbf{X}$ and it is computed as:

$$\mathbf{X}^d = \mathbf{I}^{\text{dev}}\mathbf{X}, \tag{23}$$

with:

$$\mathbf{I}^{\text{dev}} = \begin{bmatrix} \mathbf{D}^v & \mathbf{0} \\ \mathbf{0} & \mathbf{I} \end{bmatrix}$$

$$\text{with} \quad \mathbf{D}^v = \begin{bmatrix} 2/3 & -1/3 & -1/3 \\ -1/3 & 2/3 & -1/3 \\ -1/3 & -1/3 & 2/3 \end{bmatrix}; \tag{24}$$

- J_2 is the second invariant of $\mathbf{X}^d$ determined through the following formula:

$$J_2 = \frac{1}{2} \left[\left(\mathbf{X}^d \right)^{\mathsf{T}} \mathbf{M}^S \mathbf{X}^d \right]$$

$$\text{with } \mathbf{M}^S = \begin{bmatrix} \mathbf{I} & \mathbf{0} \\ \mathbf{0} & 2\mathbf{I} \end{bmatrix}. \tag{25}$$

The equation describing the associative normality rule for the internal variable is:

$$\dot{\mathbf{d}} = \dot{\zeta} \frac{\partial F \left(\mathbf{X}^d \right)}{\partial \mathbf{X}}, \tag{26}$$

with $\dot{\zeta}$ the plastic multiplier.

From the analysis of the flow rule form it can be noted that the transformation strain **d** represents a deviatoric strain, hence the condition of incompressibility during the inelastic flow is recovered. The model is completed introducing the classical Kuhn–Tucker conditions:

$$\dot{\zeta} \geqslant 0, \qquad F \leqslant 0, \qquad \dot{\zeta} F = 0, \tag{27}$$

that reduce the problem to a constrained optimization problem. The normality properties are sufficient to guarantee the satisfaction of the second principle of thermodynamics in the form of the Clausius–Duhem inequality [33]. Thus, the proposed model results are consistent with the thermodynamic formulation.

The mechanical dissipation density rate, consistent with the thermodynamically proposed formulation, is:

$$\dot{D} = \mathbf{X}^{\mathsf{T}} \dot{\mathbf{d}} \tag{28}$$

which represents the ability of the energy absorption of the material.

When a two-dimensional plane strain state is considered, with x_1–x_2 the plane of the strain, it is implicitly assumed $\varepsilon_{33} = 0$. Note that in the plane strain formulation the full three-dimensional state of stress is considered, i.e. the value of σ_{33} and X_{33} is computed and taken into account in the evolutive problem, leading to an out-of-plane transformation strain component d_{33} different from zero; thus, also in the plane strain case, the deviatoric nature of the transformation strain is preserved.

4. Numerical results

In the present section the micromechanical approach proposed above is adopted to study the overall constitutive behavior of different porous SMAs. The nonlinear micromechanical analyses are carried out implementing in the code FEAP [26] three-dimensional tetrahedral and two-dimensional plane strain quadrilateral finite elements, characterized by the SMA constitutive model described in section 3.

Three classes of problems are developed in the following in order to assess the ability of the presented model in reproducing the overall constitutive behavior of porous SMAs and in capturing their key features:

- comparison with experimental results [34] for a three-dimensional UC with a spherical pore subjected to compressive uniaxial loading–unloading history;
- influence of the porosity, considering UCs with circular section closed and open pores, characterized by different radius values;
- influence of the pore shape, considering UCs with elliptic section closed and open pores, characterized by different values of the radii ratio.

Three different types of nonlinear micromechanical analyses are performed considering three different forms of the elastic constitutive matrix:

- $\mathbf{C}(\xi)$ evaluated through a Voigt homogenization scheme, according to equation (19); these analyses are denoted in the following as FE-V;
- $\mathbf{C}(\xi)$ evaluated through a Reuss homogenization scheme, according to equation (20); the corresponding FE analyses are labeled as FE-R;
- $\mathbf{C}$ constant, i.e. not depending on the volume fraction of single-variant martensite, evaluated as the average of the $\mathbf{C}^A$ and $\mathbf{C}^S$; these analyses are identified as FE-C throughout the work.

It is worth noting that, for the latter case, a simplified form of the SMA constitutive model [24] is recovered. In fact, because of the specific form of the yield function (22), the tension-compression asymmetry is not accounted for in the present model, different to the one illustrated in [24]; this modification with respect to the original model has been introduced in order to simplify the numerical analyses. The introduced simplification will not affect significantly the results illustrated in the next sections, as only tensile or compressive loading–unloading histories will be performed, without reverse loading conditions. Indeed, except for the no porosity case, the presence of the void can lead to non-proportional loading conditions in a very small zone around the void.

In the last two classes of problems, parametric studies are conducted in order to investigate the influence of the volume fraction of voids and of their distribution and shape on the global mechanical response and on the energy absorption capability of the porous media. Since the interest is devoted to the case of periodic heterogeneous materials, repetitive UCs are considered and suitable periodic displacement boundary conditions are prescribed.

In particular, the case of closed pores is studied considering three-dimensional UCs analyzed adopting three-
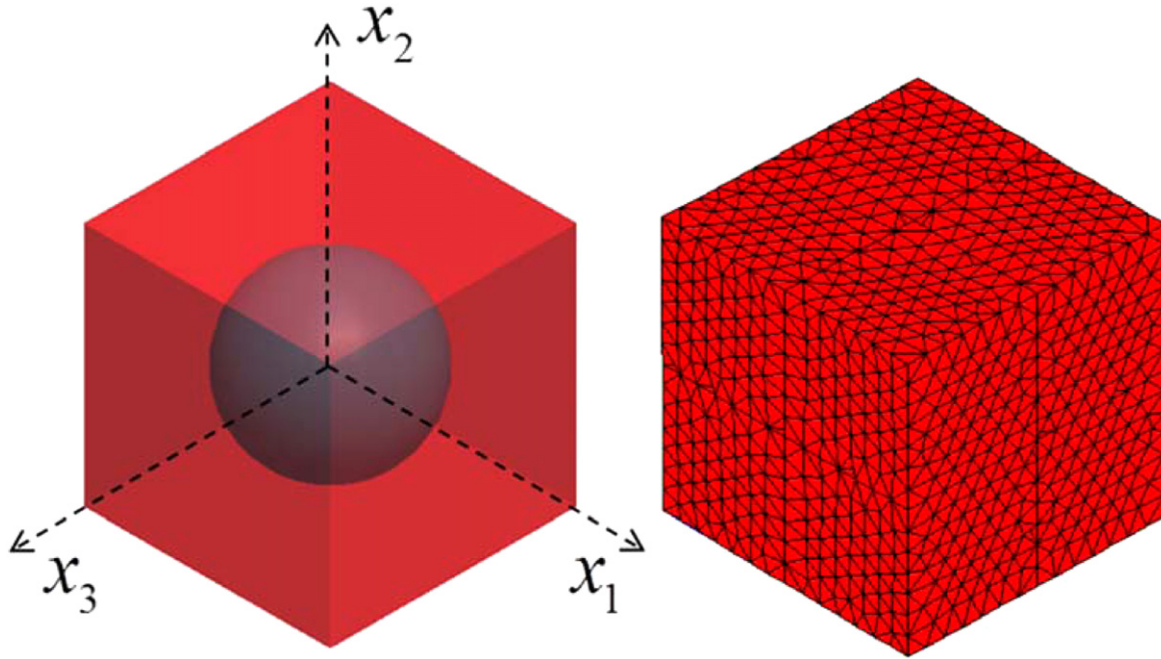
Figure 3. Porous NiTi 3D UC with spherical void ($f = 0.13$) and FE discretization.

dimensional tetrahedral elements and adopting the boundary conditions reported in equation (4). The case of open pores is investigated considering a plane strain state, which simulates the response of a thin slice of material orthogonal to the axis of the cylindrical open pore and characterized by unit thickness. In this case the boundary conditions (4) assume the explicit simplified form:

$$\tilde{\boldsymbol{u}}(a_1, x_2) = \tilde{\boldsymbol{u}}(-a_1, x_2) \qquad \forall\, x_2 \in [-a_2, a_2]$$
$$\tilde{\boldsymbol{u}}(x_1, a_2) = \tilde{\boldsymbol{u}}(x_1, -a_2) \qquad \forall\, x_1 \in [-a_1, a_1], \qquad (29)$$

On the basis of equation (28) the energy capability of the UC, evaluated at the time t, is obtained as:

$$D^{\Omega}(t) = \int_0^t \int_{\Omega} \mathbf{X}^{\mathsf{T}} \dot{\mathbf{d}}\, \mathrm{d}V \mathrm{d}\tau. \qquad (30)$$

4.1. Comparison with experimental results

The aim of this section is the assessment of the ability of the proposed model to successfully reproduce the response of porous SMAs; to this end, a comparison between the numerical results and the experimental data by Zhao *et al* [34] is performed. In [34], the dense NiTi specimens and the porous one obtained with the same SMA material, characterized by a porosity of 13%, are tested under uniaxial compression at a constant temperature $T = 58\,°\mathrm{C}$, higher than their austenite finishing temperature. In particular, the specimens are loaded up to 5% compressive strain and then unloaded, allowing the dense and the porous NiTi to exhibit the pseudo-elastic behavior.

In order to correctly describe the mechanical behavior of the porous SMA reproducing the experimental compressive

stress–strain curve, a RVE, able to retain the information of the porous medium, is examined. As the simplifying hypothesis of a regular distribution of voids is introduced (all the voids are characterized by the same dimension and shape) a three-dimensional UC made of a spherical pore (13% volume fraction) centered in a cuboidal NiTi matrix is analyzed. The nonlinear micromechanical analyses have been carried out implementing three-dimensional four-node tetrahedral elements with one Gauss quadrature point. The FE discretization of the porous UC is made of 28 856 elements and it is illustrated in figure 3, together with the UC geometry.

Since the formulation is strain driven, the average strain $\bar{\varepsilon}_{11}$ is prescribed on the UC, under suitable boundary conditions able to reproduce an uniaxial compressive test in x_1-direction. In particular, taking into account the representation form (2) for the displacement field, the following constraints are applied:

$$\tilde{u}_1(a_1, x_2, x_3) = \tilde{u}_1(-a_1, x_2, x_3) = 0$$
$$\qquad \forall\, (x_2, x_3) \in [-a_2, a_2] \times [-a_3, a_3],$$
$$u_2(x_1, a_2, x_3) = u_2(y_1, a_2, y_3)$$
$$\qquad \forall\, (x_1, x_3), (y_1, y_3) \in [-a_1, a_1] \times [-a_3, a_3],$$
$$u_2(x_1, -a_2, x_3) = u_2(y_1, -a_2, y_3)$$
$$\qquad \forall\, (x_1, x_3), (y_1, y_3) \in [-a_1, a_1] \times [-a_3, a_3],$$
$$u_3(x_1, x_2, a_3) = u_3(y_1, y_2, a_3)$$
$$\qquad \forall\, (x_1, x_2), (y_1, y_2) \in [-a_1, a_1] \times [-a_2, a_2],$$
$$u_3(x_1, x_2, -a_3) = u_3(y_1, y_2, -a_3)$$
$$\qquad \forall\, (x_1, x_2), (y_1, y_2) \in [-a_1, a_1] \times [-a_2, a_2], \qquad (31)$$
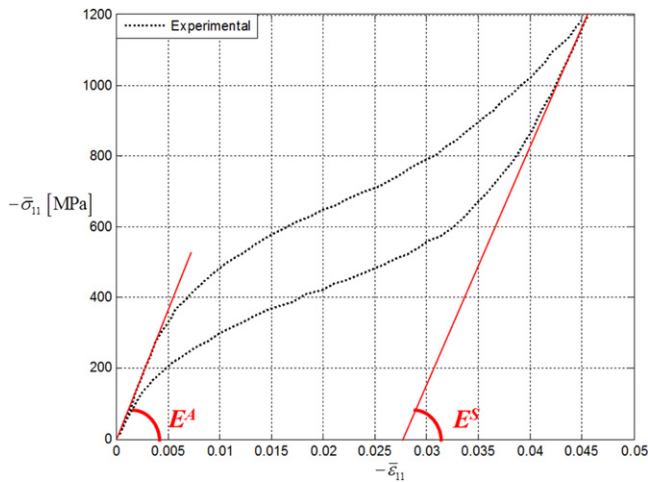
i.e. in words:

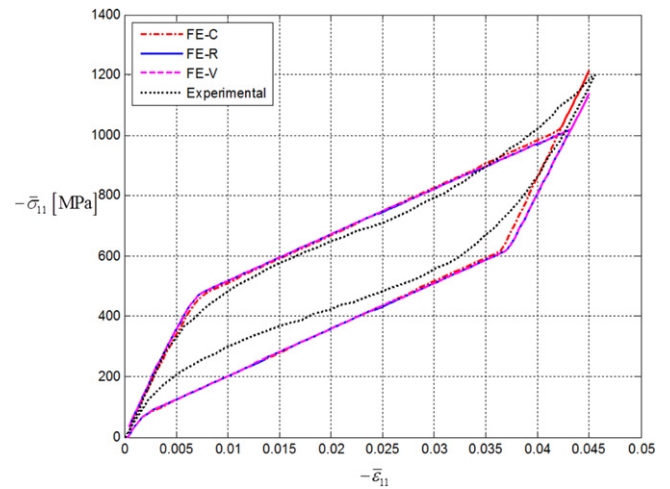**Figure 4.** Evaluation of the elastic properties of the SMA phase from the experimental results.

Figure 5. Comparison of modeling results assessed by the FE-C, FE-R, FE-V analyses and experimental stress–strain curve for dense NiTi.

- in all the nodes belonging to the external faces normal to x_1 the periodic part of the displacement is constrained along the x_1-direction;
- all the nodes belonging to the external faces normal to the x_2-direction are constrained to have the same displacement component u_2;
- all the nodes belonging to the external faces normal to the x_3-direction are constrained to have the same displacement component u_3.

Notably, three types of analyses are developed hereinafter adopting the SMA constitutive model with a constant elastic tensor $\mathbf{C}$ and with $\mathbf{C}(\xi)$, evaluated through the Reuss and Voigt homogenization schemes and able to account for the phase transformation from austenite or multi-variant martensite to single-variant martensite.

The material parameters are calibrated starting from the mechanical properties of dense NiTi reported in [34]. The Young moduli of austenite and single-variant martensite phases are estimated from figure 4, where the experimental stress–strain curve of the dense SMA specimen is illustrated. The assumption that dense NiTi is fully transformed into single-variant martensite at the end of the loading step is made.

The mechanical properties are listed in table 1. Specifically, the symbols E^A and ν^A indicate the Young modulus and the Poisson ratio, respectively, when the volume fraction of the single-variant martensite in the SMA is zero ($\xi = 0$) and only the austenitic phase is present; the Young modulus and the Poisson ratio when the SMA is fully transformed in single-variant martensite ($\xi = 1$) are denoted with the symbols E^S and ν^S.

In particular, the martensite finishing temperature is set according to the transformation temperatures provided by [34] for the dense NiTi. The other input material parameters of the model, i.e. h, β, ε_L and σ_y, are calibrated in order to fit the experimental compressive stress–strain curve of the dense NiTi specimen. It can be noted that, according to the model described in section 3, the same threshold value σ_y is assumed

for the uniaxial critical stresses in tension and in compression evaluated at $T \leqslant M_f$.

For the nonlinear micromechanical analysis FE-C, a unique Young modulus $E = 70\,500$ MPa and a unique Poisson ratio $\nu = 0.33$ are evaluated as the average means of the correspondent moduli of the austenitic and single-variant martensite phases reported in table 1.

The response of the UC made of dense NiTi, i.e. $f = 0$, and subjected to the compressive average strain history $\left(-\bar{\varepsilon}_{11} = 0.045\right)$ is illustrated in figure 5, where the comparison with the experimental curve of Zhao *et al* [34] is reported in terms of the average compressive stress $\bar{\sigma}_{11}$ versus the average compressive strain $\bar{\varepsilon}_{11}$ for the FE-C, FE-V and FE-R analyses. From figure 5 it can be observed that the FE-C approach provides a good approximation of the experimental data for the dense SMA, reproducing the pseudo-elastic effect, as the austenite and martensite elastic moduli are very close.

In this case two different Young moduli and Poisson ratios are considered for the austenitic and single-variant martensite phases, i.e. performing the FE-V and FE-R analyses, the pseudo-elastic effect is recovered and the initial stiffness is captured together with the starting point of the forward martensitic transformation. The maximum value of the average stress achieved at the end of the loading step is slightly overestimated by the FE-C analysis and underestimated by the FE-V and FE-R analyses.

Once the material parameters are set for the dense NiTi, the mechanical behavior of the porous SMA with a porosity level of 13% is investigated, performing a micromechanical analysis in which the porous UC is considered. In particular, a monotonic increasing value of the average strain is prescribed on the porous NiTi UC until the value $-\bar{\varepsilon}_{11} = 0.045$ is reached.

The mechanical responses of the porous UC subjected to uniaxial compression, obtained carrying out the FE analyses, are plotted in terms of the average stress $-\bar{\sigma}_{11}$ versus the
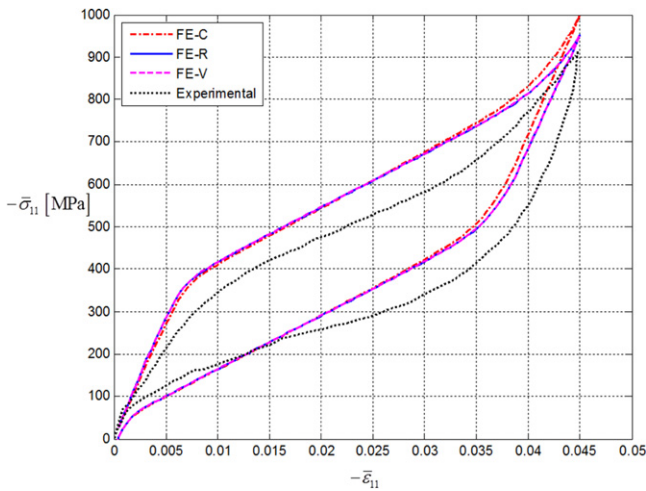
Figure 6. Comparison of modeling results assessed by the FE-C, FE-R, FE-V analyses and experimental stress–strain curve for porous NiTi ($f = 0.13$).

average strain $-\bar{\varepsilon}_{11}$ in figure 6, where they are compared with the stress–strain curve given by the experimental compressive test.

The average stress corresponding to the starting of the austenite–martensite transformation is overestimated by the FE-C, FE-V and FE-R results, the maximum average stress achieved at the end of the loading phase is overestimated by the FE-C analysis, while it is almost accurately evaluated by the FE-V and FE-R.

However, the performed analyses FE-C, FE-V and FE-R provide a good approximation of the experimental data and all the results confirm the capability of the proposed procedure of accurately predicting the stress–strain of porous SMA, only on the basis of the constitutive model parameters of the dense counterpart, which are in reduced number and which can be easily identified by few and simple experimental tests in a reliable way.

4.2. Closed pore

The case of closed pores (see, e.g. [35]) is investigated, considering a three-dimensional UC with a void centered in a NiTi matrix; the influence of the porosity and of the void shape on the overall mechanical response of the porous material is evaluated. In particular, the dissipation capacity of the material is computed for loading-unloading histories. Computations are performed adopting four-node tetrahedral elements with almost regular meshes characterized by the ratio size of the element over the UC edge of about 0.03. Initially, a UC with a spherical void is studied considering different porosities; then, the transition from the spherical (closed) to the cylindrical (open) shape of the pore is numerically analyzed.

The material properties of the dense SMA are the ones adopted in [24] and are reported in table 2. According to the formulation of the proposed constitutive model for the dense SMA, which accounts for the volume fraction of the single-

variant martensite, different elastic moduli are considered for the SMA phases of austenite and single-variant martensite.

The pseudo-elastic loading-unloading history, reported in table 3, is prescribed, applying an increasing value of the tensile average strain $\bar{\varepsilon}_{11}$ in the UCs until the value $\eta = 0.02$ is reached at a constant temperature $T = 270$ K, greater than the temperature A_f at which the more-ordered austenitic phase is stable. Then, the NiTi pseudo-elasticity is exploited unloading the UC and, thus, allowing the complete recovery of the transformation strain in the porous SMA. During the whole loading history the other average strain components are kept equal to zero. Thus, the loading history is uniaxial in terms of the average strain.

The above loading history is prescribed on the UCs characterized by the different volume of voids and shapes, developing nonlinear micromechanical finite element analyses considering the Reuss scheme for the evaluation of the elasticity matrix (FE-R).

4.2.1. Influence of the porosity. A cubic three-dimensional UC with a centered spherical void is studied; five different porosities are investigated, considering the following values of void volume fraction f: 0, 0.10, 0.154, 0.20 and 0.35, obtained considering different values of the radius R and keeping constant the side $a_1 = a_2 = a_3$ of the UC.

In figure 7 the mechanical response of the porous SMA is reported in terms of average stress $\bar{\sigma}_{11}$ versus the average strain $\bar{\varepsilon}_{11}$ for all the studied porosities, when it is set $\eta = 0.02$. It can be pointed out that, as expected, the value of the maximum average normal stress along the x_1-direction $\left(\bar{\sigma}_{11}{}^{\max}\right)$, reached at the end of the loading step, decreases for increasing values of the porosity.

Note that the mechanical responses of the dense and porous SMA correspond to the uniaxial strain loading history, above described, and result in a significant difference from the case of uniaxial stress. In fact, the stress components σ_{22} and σ_{33}, not herein reported, have the same order of magnitude of σ_{11} at the end of the loading phase, i.e. when the maximum value of the stress σ_{11} is very high. The presence of σ_{22} and σ_{33} together with σ_{11} induces a low value of the second invariant of the deviatoric stress, J_2, often considered responsible for plastic flow. Thus, in this case, neglecting the plastic effect could be considered a reasonable assumption.

The influence of the porosity on the energy absorption capability of the porous SMA, when the pseudo-elastic effect occurs in the material, is studied. In figure 8(a) the energy dissipated in the UC per unit volume of the solid fraction is plotted in function of the porosity with red triangles. The energy dissipated in the dense SMA is also represented with a blue square.

It can be pointed out that for all the studied porosities the dissipated energy per solid volume is higher than the energy dissipated by the dense SMA and the maximum value of the dissipated energy per solid volume, obtained for $f = 0.10$, is more than twice the value for the dense SMA. As the volume of voids continues to increase, the dissipated energy per volume tends to decrease, with a value for $f = 0.35$ which

Table 1. Material properties of the NiTi specimen subjected to uniaxial compression.

NiTi matrix mechanical properties				
$E^A = 75\,000$ MPa	$\nu^A = 0.33$	$E^S = 66\,000$ MPa	$\nu^S = 0.33$	$h = 13\,500$ MPa
$\beta = 6$ MPa K^{-1}	$\varepsilon_L = 0.034$	$M_f = 296.24$ K	$\sigma_y = 200$ MPa	

remains significantly higher than the one obtained for the case of dense SMA ($f = 0$). In figure 8(b), the average value $\bar{\bar{\xi}}$ of the single-variant martensite volume fraction ξ per solid volume is plotted versus porosity with red triangles. The value of $\bar{\bar{\xi}}$ for solid volume for the dense SMA is represented with a blue square. It can be pointed out that $\bar{\bar{\xi}}/(1 - f)$ has the same trend respect to porosities obtained for the dissipation for solid volume, represented in figure 8(a). In fact, the maximum value of $\bar{\bar{\xi}}/(1 - f)$ is obtained for $f = 0.10$, while it tends to decrease with the increasing of porosity.

4.2.2. Transition from closed to open pores. The transition from closed to open (interconnected) pores is investigated studying UCs with an ellipsoidal void, keeping constant the side $a_1 = a_2 = a_3$. In particular, different shapes of void are considered in the analyses, from spherical to cylindrical with axis x_3 orthogonal to the prescribed uniaxial average strain $\bar{\varepsilon}_{11}$, as schematically illustrated in figure 9. For the ellipsoidal void it is set: a the radius along x_1-direction, b the radius along x_2-direction and c the radius along x_3-direction. Thus, starting from a UC characterized by $f = 0.154$ and by a spherical void, i.e. $a = b = c$, keeping $a = b$ and changing only c, the following UCs are obtained:

- UC with spherical closed void with $c = a$ and $f = 0.154$;
- UC with ellipsoidal closed void with $c = 1.25\,a$ and $f = 0.179$;
- UC with ellipsoidal closed void with $c = 1.5\,a$ and $f = 0.216$;
- UC with ellipsoidal open void with $c = 1.75\,a$ and $f = 0.246$;
- UC with cylindrical open void with $c \to \infty$ and $f = 0.35$.

The loading history, reported in table 3, is prescribed to all the UCs.

In figure 10 the average stress $\bar{\sigma}_{11}$ versus the average strain $\bar{\varepsilon}_{11}$ for all the studied UCs is reported. It can be pointed out that the transition from a closed to an open pore induces a reduction of the phase transformation activation stress, of the achieved maximum stress and of the stress–strain slope during the austenite–martensite transformation. This reduction is due to two causes: the geometrical change of the pore shape from closed to open and the increasing of porosity.

To better understand the effect of these two causes on the mechanical response, the stress–strain curves in the x_1-direction of the two cells, with $f = 0.35$ and characterized by

the closed spherical or open cylindrical void, are compared in figure 11. It can be noted that the maximum stress $\left(\bar{\sigma}_{11}{}^{\max}\right)$, achieved at the end of the loading phase, is almost the same for the two cells. On the other hand, in the case of the open void, the activation stress results are lower while the slope of the stress–strain curve during the phase transformation results are higher with respect to the closed pore.

The effect of the transition shape from closed to open pore on the energy absorption capability is also investigated. In figure 8(a) the dissipated energy for solid volume is plotted with green circles for all the studied cells. It can be pointed out that the dissipated energy for solid volume is maximum for the UC with a spherical void and tends to decrease, from closed to open pores, keeping a value always higher than the dissipated energy per solid volume evaluated for the dense SMA (blue square). This reduction is due again to the increasing of porosity and to the pore shape change. It can be noted that for the porosity $f = 0.35$ the dissipated energy is higher for the cell with a closed spherical pore than for the cell with an open cylindrical pore.

It could be remarked that these considerations are related to the specific prescribed boundary and loading conditions. Qidwai *et al* [11] presented a comparison of the overall stress–strain response for closed and open porosity, considering boundary and loading histories, different from the ones herein prescribed. For this reason their results are not always in agreement with the one presented in this section.

4.3. Open pore

The case of interconnecting open porous SMA is considered, i.e. it is assumed that the pores have a cylindrical shape. This study is of particular interest as the case of interconnecting pores is very common, mainly for greater values of the porosity [36, 37]. Moreover, it appears very interesting to evaluate the response of the porous alloy in the direction orthogonal to the cylindrical pore, as in this case the stress distribution and, as a consequence, the transformation strain distribution is strongly influenced by the presence of the pore. Computations are performed considering the same material properties introduced for the case of closed pores.

In order to perform the FE-C analyses a Young modulus $E = 53\,000$ MPa and a Poisson ratio $\nu = 0.36$ are considered, evaluated as the average of the correspondent moduli of the austenite and single-variant martensite phases.
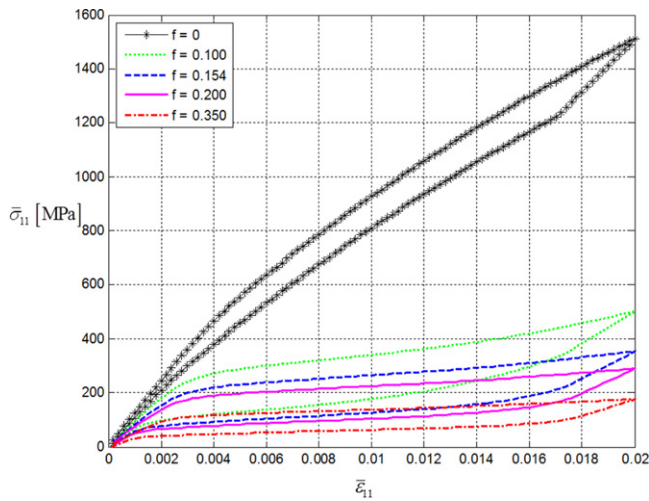
4.3.1. Influence of the porosity. In the following applications the influence of the porosity on the macroscopic mechanical

Table 2. Material properties for dense NiTi.

NiTi mechanical properties			
$E^A = 75\,000$ MPa	$\nu^A = 0.36$	$E^S = 31\,000$ MPa	$\nu^S = 0.36$
$h = 1000$ MPa	$\beta = 2.1$ MPa K^{-1}	$\varepsilon_L = 0.06$	$M_f = 223$ K
$\sigma_y = 61.23$ MPa			

Table 3. Loading–unloading history for the porous NiTi.

t (s)	0	1	2
$\bar{\varepsilon}_{11}$	0	η	0
T (K)	270	270	270

Figure 7. Response of the porous UCs with a spherical void along x_1-direction for $\eta = 0.02$.

response and on the energy dissipation capability of porous NiTi is investigated. The simplifying hypothesis of a regular distribution of circular voids in the material is introduced, considering a square periodic UC with a circular centered void, as shown in figure 12. The study is conducted in two-dimension using plane strain conditions, which simulate the response of a slice of unit thickness of a solid characterized by a cylindrical pore orthogonal to the plane of interest.

The nonlinear micromechanical analyses are carried out using four-node quadrilateral finite elements. In order to examine several levels of porosity f, different values of the radius R of the pore are set, keeping constant the side of the UC, i.e. $a_1 = a_2$. Specifically, seven UCs are considered, characterized by the following values of void volume

fraction: 0, 0.05, 0.10, 0.20, 0.35, 0.45 and 0.55. Of course, the UC with $f = 0$ degenerates to the case of dense SMA.

The FE discretization of the porous UC is made using a structured mesh characterized by the ratio size of the element over the UC edge of about 0.02.

Two different loading histories (table 3) are prescribed on the examined UCs in order to activate the pseudo-elastic effect in the porous SMA. For the first loading history it is set $\eta = 0.02$, while for the second one it is $\eta = 0.04$.

The above loading histories are prescribed on the seven UCs characterized by the different volume of voids and for each UC the three forms of the constitutive matrix are considered adopting the model discussed in section 3 and, thus, developing nonlinear micromechanical finite element analyses indicated as FE-V, FE-R and FE-C.

Figure 13 shows the behavior of all the UCs in terms of the average normal stress $\bar{\sigma}_{11}$ versus the average strain $\bar{\varepsilon}_{11}$ for both the loading cases characterized by different values of the maximum average strain prescribed at the end of the loading phase, i.e. 2% (figure 13(a)) and 4% (figure 13(b)). Results are plotted for porosity values equal to 0, 0.10, 0.35, and 0.55; computations for porosities equal to 0.05, 0.20 and 0.45 are also performed but their results are omitted in order to make the figures clearer.

The same observations, presented in the previous subsection for the closed pore UCs, can be drawn for the case of an open pore. In fact, it can be pointed out that for both the loading histories the value of the maximum average normal stress along the x_1-direction $\left(\bar{\sigma}_{11}^{\text{ max}}\right)$, reached at the end of the loading step, decreases for increasing values of the volume of voids. Furthermore, figure 13 highlights that for increasing porosity levels the stress–strain slope during the austenite–martensite phase transformation and the activation stress significantly reduce.

From figure 13, it can be also noticed that the use of the three different forms of the elastic constitutive matrix leads to the same qualitative behavior of the porous SMA. For dense SMA, the difference between the results obtained for a constant or variable elastic matrix can be significant. In fact, for low values of the prescribed strain, FE-C leads to a less stiffer response than FE-R and FE-V; on the contrary, increasing the prescribed strain (figure 13(b)), the FE-C leads to stiffer results, due to the phase transformation evolution.
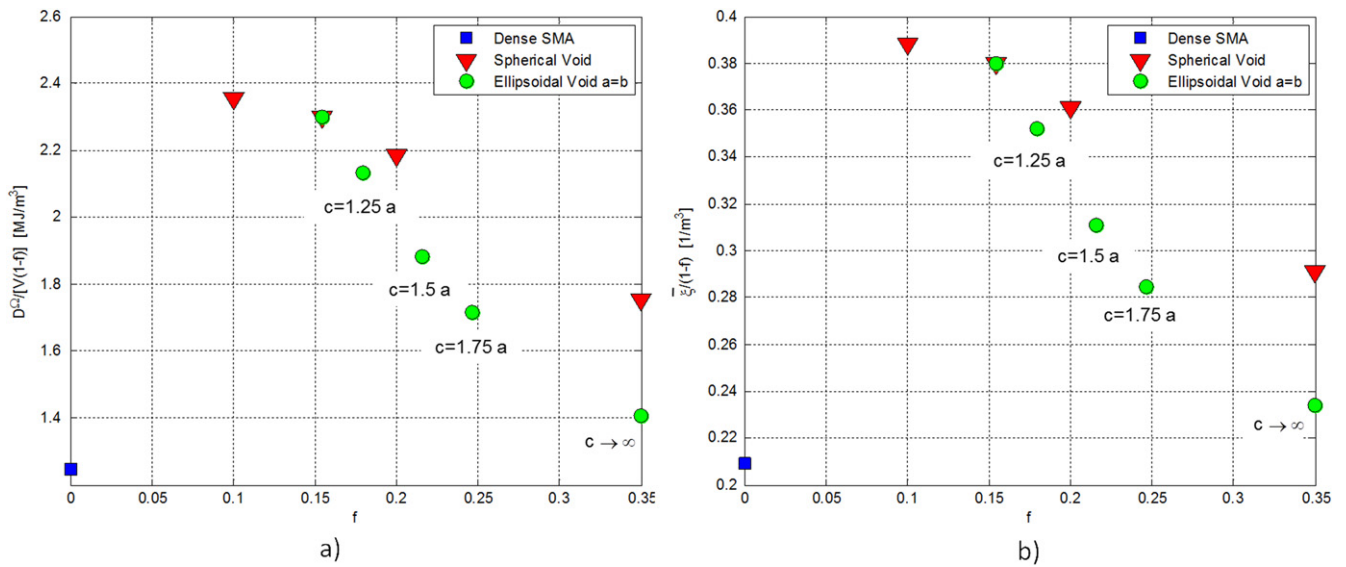
Figure 8. Dissipated energy per solid volume (a) and average of single-variant martensite volume fraction for solid volume (b) versus porosity for UCs with a spherical and ellipsoidal void.
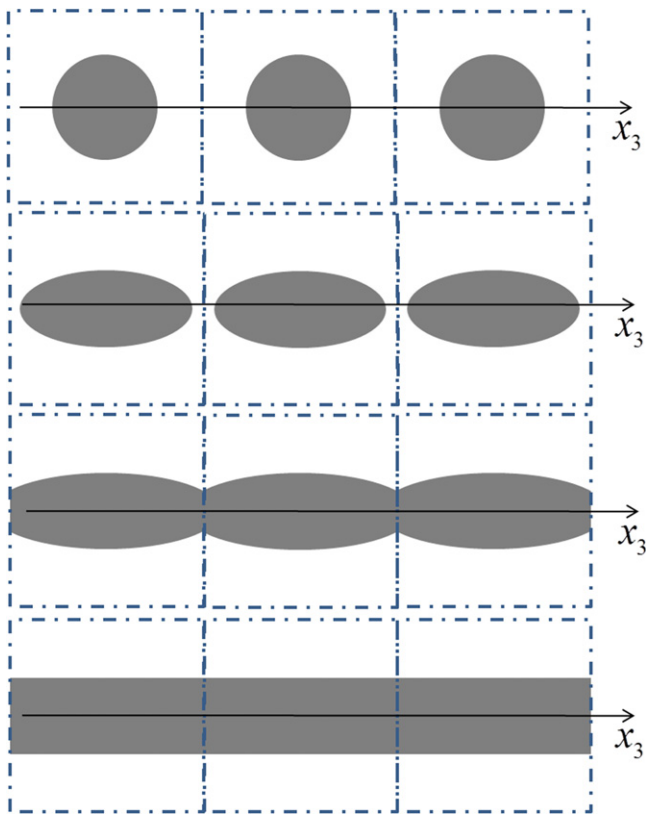

Figure 9. Transition from closed to open pore.
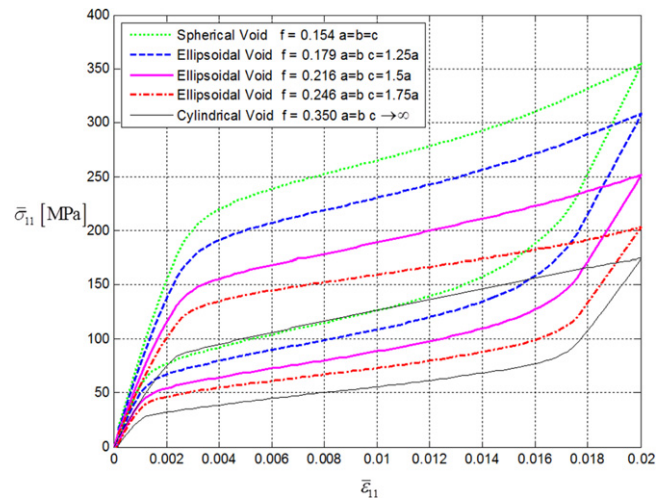

Figure 10. Response of the porous UCs with an ellipsoidal void for shapes from spherical to cylindrical.
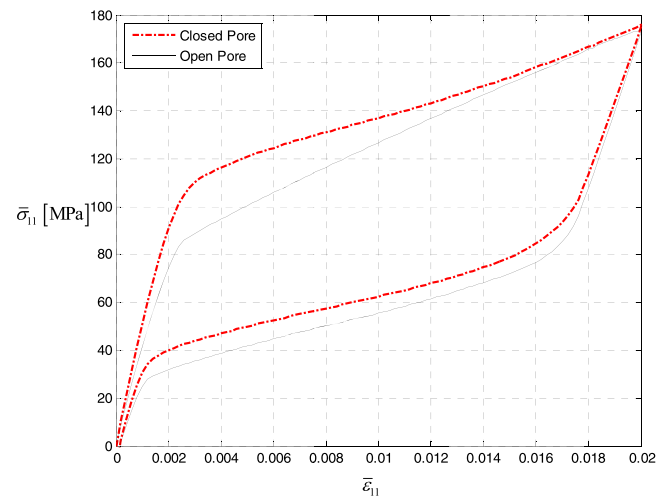
Figure 11. Response of two UCs with $f = 0.35$ characterized by a closed spherical pore and an open cylindrical pore.
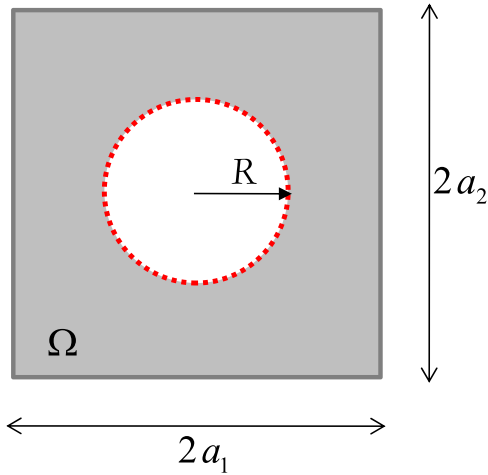
This effect is due to the fact that the constant elastic modulus for the FE-C results are lower than the austenite modulus at the beginning of the loading history, while the results are greater than the martensite modulus when the phase transformation evolves. For low values of the porosity, this effect is evident for both $\eta = 0.02$ and $\eta = 0.04$, as the phase transformation occurs also for lower average strain values

Figure 12. Porous NiTi periodic 2D-UC with a cylindrical void with circular directrix.
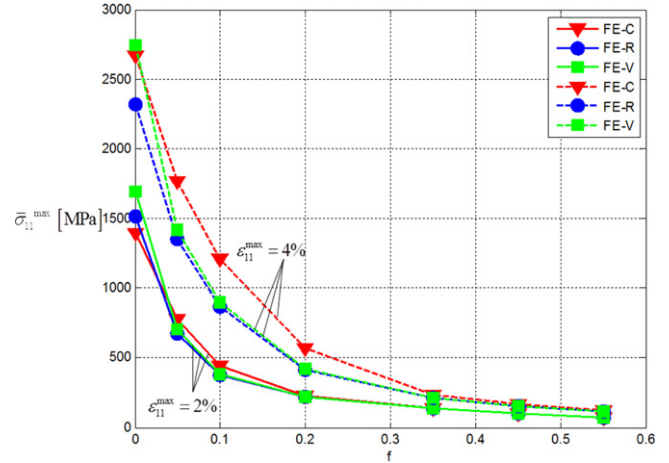

Figure 14. Maximum average normal stress obtained for a prescribed maximum average strain equal to 2% and 4%.
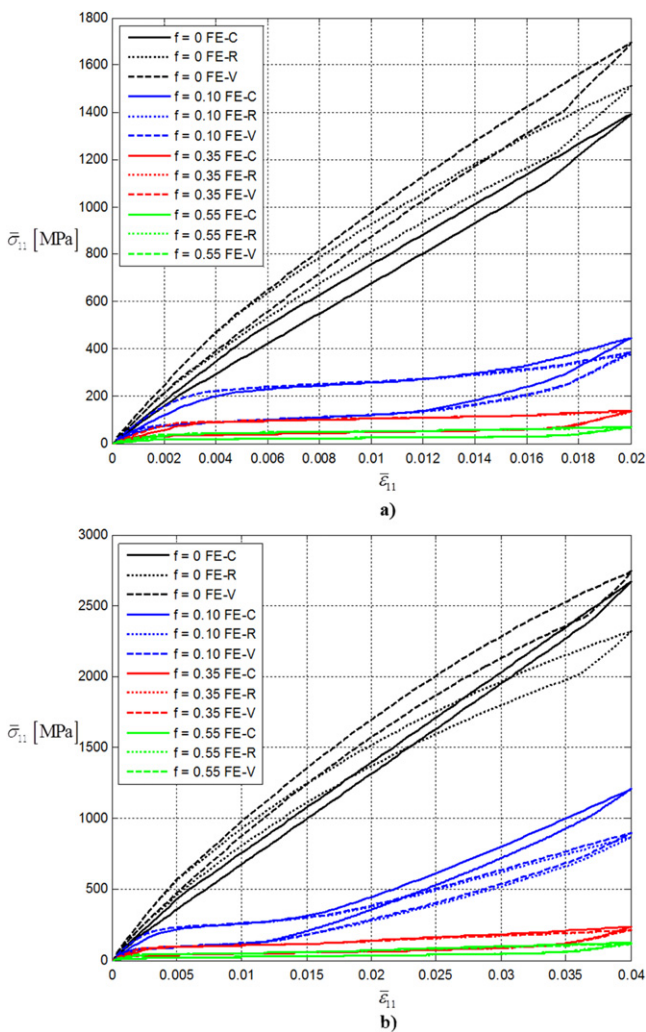

Figure 13. Responses of the porous UCs along x_1-direction for a prescribed maximum average strain equal to 2% (a) and 4% (b).

with respect to the dense SMA. With the increasing of the porosity, the effect becomes less important because the presence of the void significantly reduces the overall stiffness of the UC.

The analysis of the trend of the maximum value of the average normal stress along the x_1-direction, achieved for the different values of f, is illustrated in figure 14 for all the FE-V, FE-R and FE-C analyses and for both the two levels of the prescribed average strain. In details, the results given by the first loading history are reported with solid lines, while the curves of the second loading case are represented by dashed lines. Furthermore, the values of the maximum average stress $\left(\overline{\sigma}_{11}{}^{\max}\right)$ obtained by the FE-V analyses are shown with the square green symbols, by the FE-R analyses with round blue markers and the FE-C simulations with red triangles. Summarizing, taking into account the observations made for figure 13, figure 14 highlights that:

- for the same porosity f, the value of the maximum average tensile stress is obviously higher for the analyses in which the average strain reaches the value of $\eta = 0.04$, for all the FE-V, FE-R and FE-C analyses;
- for all the FE-V, FE-R and FE-C simulations, the difference between the values of $\left(\overline{\sigma}_{11}{}^{\max}\right)$ for the two loading histories tends to decrease with the increasing of porosity, so that for a high level of void fraction the increase of the average strain leads to a low increase of the maximum tensile average stress;
- for $\eta = 0.02$ and for $\eta = 0.04$ with $f > 0.30$, FE-V, FE-R and FE-C lead to very closed results; while for low value of the porosity FE-C provides higher values of the maximum stress.

As noted for the three-dimensional analyses, also for the two-dimensional ones the stress components σ_{22} and σ_{33}, not herein reported, have the same order of magnitude of σ_{11} at the end of the loading phase; thus, also in this case, the plastic effect could be neglected.
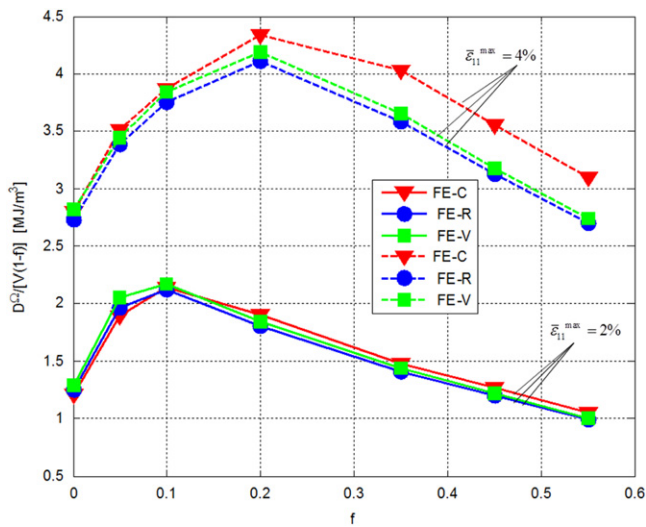
Figure 15. Dissipated energy per solid volume obtained for a prescribed maximum average strain equal to 2% and 4%.

The incidence of the volume fraction of voids on the energy absorption capability of the porous SMA, exploiting the pseudo-elastic effect, is also investigated for the considered loading histories and for all the performed FE analyses. The energy dissipated in the UC per unit volume of the solid fraction is evaluated and plotted in figure 15 in function of the porosity for the two considered values of η.

From figure 15 it can be emphasized that for all the FE-V, FE-R and FE-C simulations, the energy dissipated per volume of the slice of unit thickness of the solid during the pseudo-elastic loading cycle increases for higher values of the prescribed maximum overall strain, as expected. For all the studied porosities the dissipated energy per solid volume is higher than the energy dissipated by the dense SMA, except for the UC with $f = 0.55$. In particular, the FE-V, FE-R and FE-C analyses provide very closed results for $\eta = 0.02$, while for $\eta = 0.04$ and $f > 0.20$, the FE-C analyses tend to provide higher values of the dissipated energy, even if the trend for the three types of analyses is the same. This effect is due to the increasing of the material in the UC involved in the phase transformation for high average strain and high porosity.

The maximum value of the dissipated energy per solid volume, that is almost one and a half the value obtained for the dense SMA, is reached for $f = 0.10$ when $\eta = 0.02$ and $f = 0.20$ when $\eta = 0.04$.

As the value of the volume of voids increases, the dissipated energy per volume of the slice of unit thickness of the solid tends to decrease, with a value for $f = 0.55$ slightly smaller than the one obtained for the case of dense SMA, except for the FE-C analysis with $\eta = 0.04$. The FE-C results appear less reliable with respect to FE-R and FE-V as they are obtained assuming equal moduli for the austenite and martensite. This effect is due to the increasing of the material involved in an advanced phase transformation for increasing values of the average prescribed strain and of porosity; in these cases FE-C analyses lead to a stiffer response during the

loading phase with respect to FE-R and FE-V, as has already been discussed.

In figure 16 the distribution maps of the volume fraction of the single-variant martensite ξ in a SMA RVE is plotted for the FE-R analyses at the end of the two loading cases for three different values of porosities: $f = 0.05$, $f = 0.20$ and $f = 0.55$. The results of the dissipation for the different values of the porosity, reported in figure 15, can be interpreted looking at the distribution of the martensite volume fraction illustrated in figure 16. In particular, with reference to the case $\eta = 2\%$, it can be observed that the area where the transformation is almost completed is quite the same for $f = 0.05$ and $f = 0.20$, while it is significantly smaller for $f = 0.55$; in fact, the dissipation reduces for higher value of the porosity with respect to the cases $f = 0.05$ and $f = 0.20$. Moreover, similar considerations can be drawn for $\eta = 4\%$, except for $f = 0.20$ where figure 16(b) shows that the area interested by a complete transformation is wider with respect to the other porosities, leading to a significantly higher dissipation.

It can be pointed out that for this overall uniaxial strain history, at the increasing of porosity, the size of the UC part where the phase transformation occurs decreases leaving a greater part of the UC with almost a linear elastic behavior. As a consequence, the dissipated energy over the SMA volume tends to decrease and the material is not well exploited for energy absorption.

Then, the third loading history reported in table 4 is considered for the UC, characterized by the same value of the strain $\bar{\varepsilon}_{11}$ and $\bar{\varepsilon}_{22}$ with the other average strain components equal to zero.

In figure 17 the distribution map of ξ is plotted for the FE-R analyses at the end of the loading case for three different values of porosities: $f = 0.05$, $f = 0.20$ and $f = 0.55$. It can be pointed out that for this loading condition also for high values of porosity the greater part of the UC is undergoing transformation strains, thus the material is able to dissipate a greater amount of energy with respect to the uniaxial strain case.

In figure 18 the dissipated energy per volume of the slice of unit thickness of the solid is plotted versus the porosity for the FE-C, FE-R and FE-V analyses for the third loading history, providing very close results. It can be pointed out that the energy dissipated by the dense SMA is almost the same as in the previous loading path with $\eta = 0.04$, while the dissipated energy per solid volume for all the studied porosities is significantly higher than for the previous two loadings. This is due to the wider UC part involved in the phase transformation. The maximum value of the dissipated energy per solid volume is almost two times higher than the one obtained for the dense SMA and it is reached for $f = 0.35$ while with increasing porosity it decreases very slightly.

In the same figure the dissipated energy per UC volume is plotted for FE-C, FE-V, FE-R analyses. It can be noted that also in this case the density of dissipated energy is higher than the case of dense SMA. Increasing the porosity over than 0.10 the dissipated energy per UC volume starts to decrease reaching a value lower than the dense SMA for about $f = 0.5$.
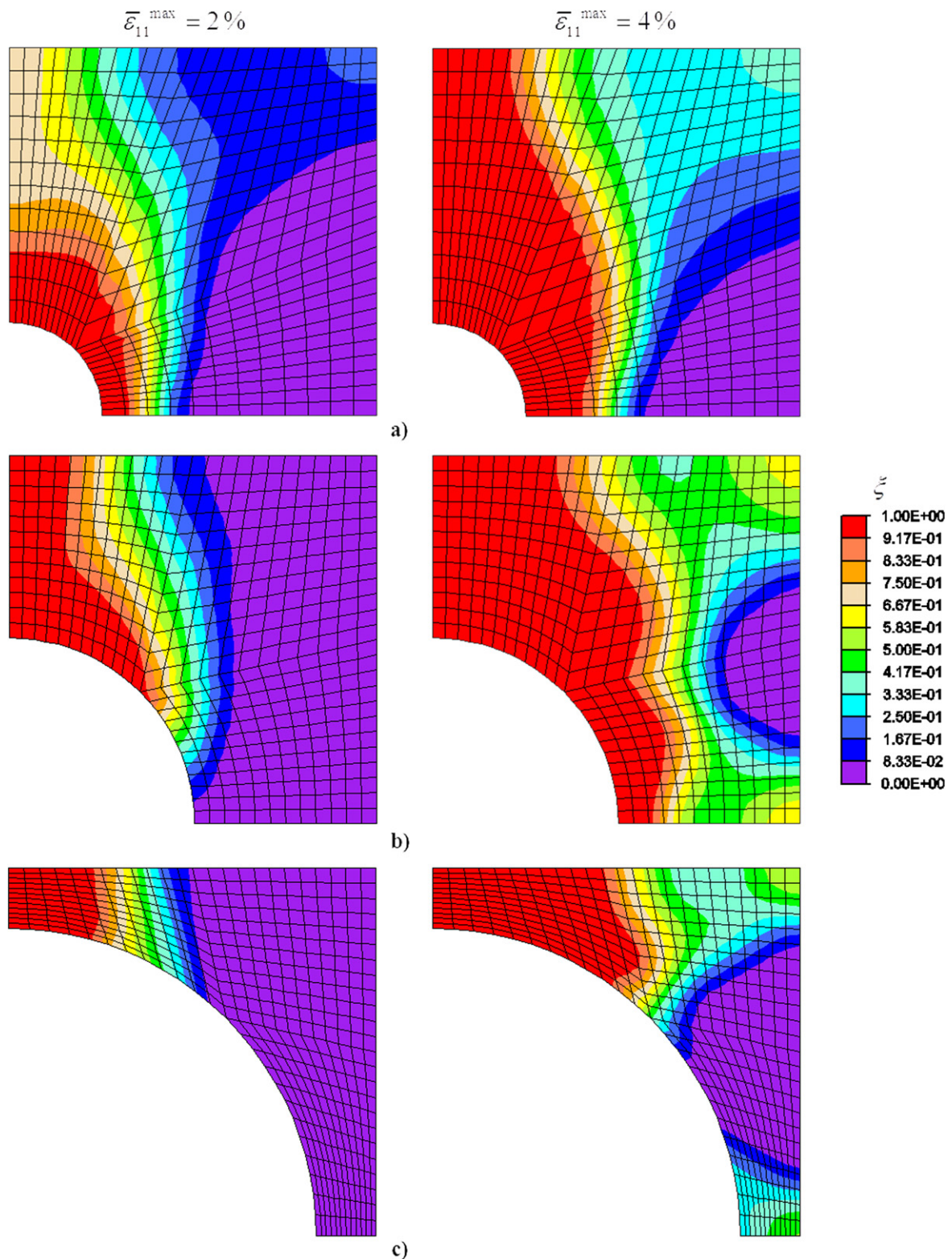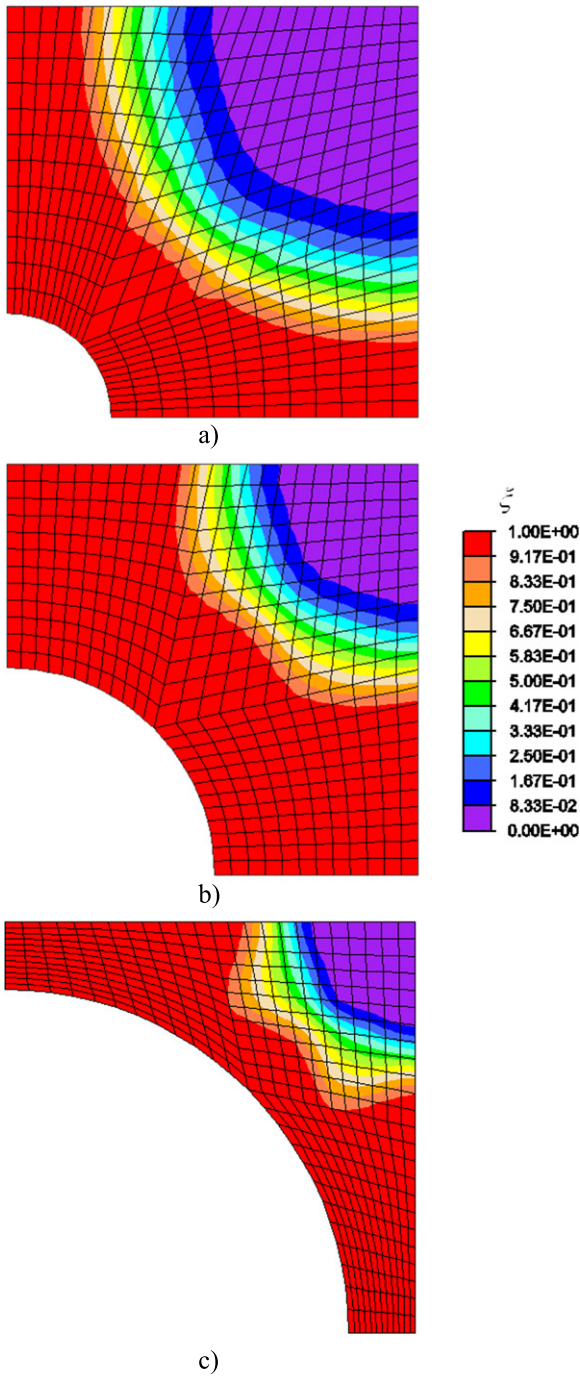
Figure 16. Volume fraction of single variant martensite evaluated in the analyses FE-R at the end of the loading step ($t = 1$ s) in a quarter of the UC with $f = 0.05$ (a), $f = 0.20$ (b), $f = 0.55$ (c) for the first and the second loading histories.

4.3.2. Influence of the pore shape. The aim of the second numerical simulation is to investigate the effect of the shape and orientation of the voids on the mechanical response of porous SMAs and on their ability to dissipate energy. For this purpose a parametric study on a porous SMA is conducted. In particular, a two-dimensional square UC made of a NiTi matrix characterized by the same material properties of the previous application (table 2) is considered. An elliptical void

Table 4. Third loading history for the porous NiTi with circular void.

t (s)	0	1	2
$\bar{\varepsilon}_{11}$	0	0.04	0
$\bar{\varepsilon}_{22}$	0	0.04	0
T (K)	270	270	270

a)

b)

c)

Figure 17. Volume fraction of single variant martensite evaluated in the analyses FE-R at the end of the loading step ($t = 1$ s) in a quarter of the UC with $f = 0.05$ (a), $f = 0.20$ (b), $f = 0.55$ (c) for the third loading history.
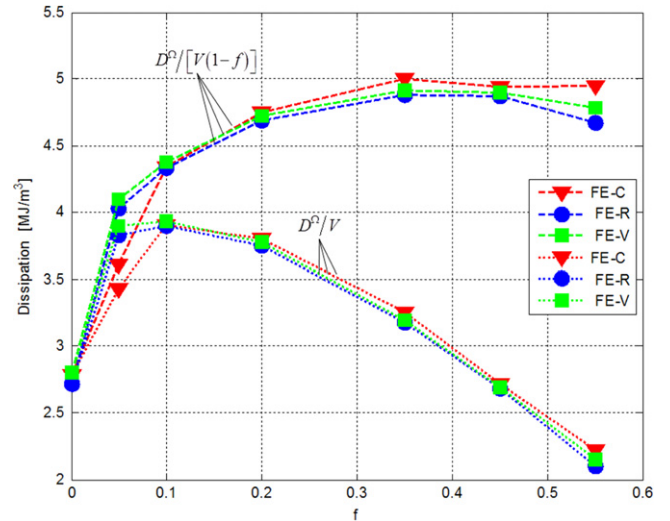

Figure 18. Dissipated energy obtained for the third loading history.
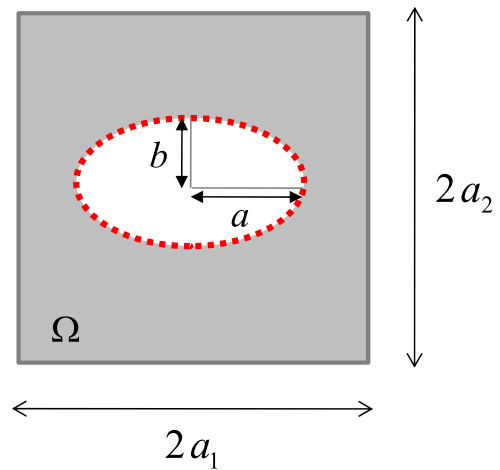

Figure 19. Porous NiTi periodic 2D-UC with a cylindrical void with elliptic directrix.

is centered in the periodic UC, being a the radius along the x_1-direction and b the radius along the x_2-direction. In figure 19 the geometry of the considered UC is illustrated.

Three values of porosity are chosen setting f equal to 0.10, 0.20 and 0.35 and for each porosity level seven different values of the ratio a/b are considered. In particular, varying the size of the radii of the elliptical void the following values for the ratio a/b are analyzed: 0.50, 0.57, 0.67, 1, 1.50, 1.75, 2. It is worth noting that the UCs characterized by the ratios 1.50, 1.75, 2 can be obtained rotating the elliptic pore by $\pi/2$ of UCs with a/b equal to 0.50, 0.57 and 0.67, respectively. Obviously the elliptical pore with the ratio $a/b = 1$ degenerates in the case of the circular hole in a NiTi matrix, discussed in the previous application.

The UC is discretized using a structured mesh characterized by the ratio size of the element over the UC edge of about 0.02 for all the porosities and the all values a/b.

The mechanical response of the heterogeneous media, when the pseudo-elastic effect is activated, is investigated. Thus, the same loading history defined in table 3 with
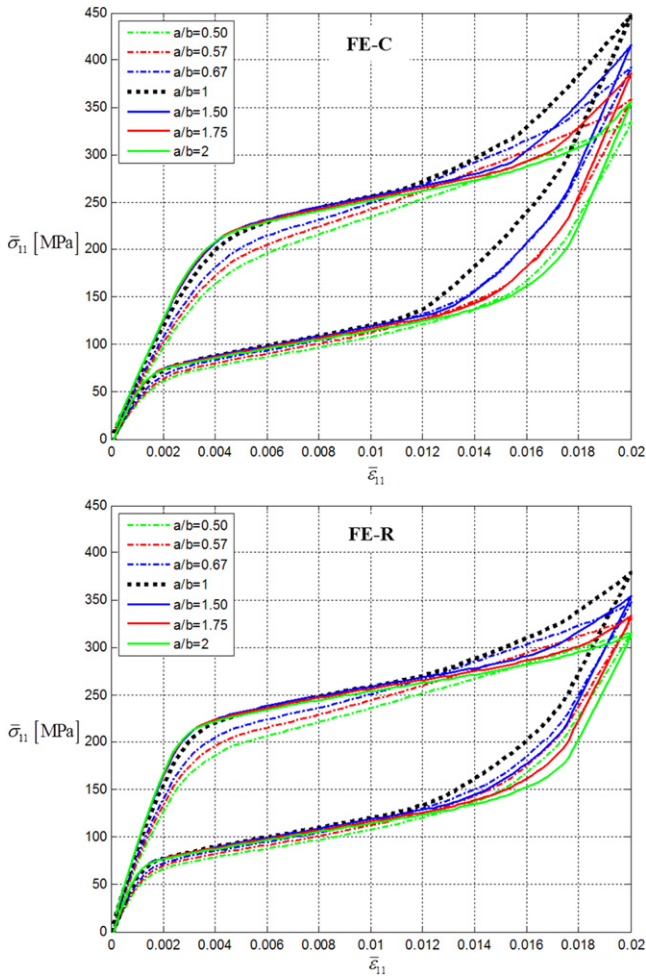
Figure 20. Mechanical responses of the porous UCs with elliptical voids for $f = 0.10$.

Figure 21. Mechanical responses of the porous UCs with elliptical voids for $f = 0.20$.

$\eta = 0.02$ is prescribed on all the UCs characterized by different porosities and different geometries. FE-C and FE-R analyses are performed for all the porosities and the ratios a/b.

The overall constitutive behaviors are plotted in terms of average normal stress versus the average normal strain along the x_1-direction for $f = 0.10$, $f = 0.20$ and $f = 0.35$ in figure 20, figure 21 and figure 22, respectively. In details, in all the graphs the responses for the three UCs are plotted with square black dots for the ratio $a/b = 1$ (i.e. UCs with circular voids), dashed lines for pores with $a < b$ and solid line for pores $a > b$.

It can be noted that, according to the loading history, the applied average strain is prescribed along the x_1-direction. Thus, for the UCs with $a > b$ the load is assigned along the direction of the major radius of the void, while for the cases $a < b$ the average strain is applied along the direction of the minor radius of the ellipse.

From figure 20, figure 21, and figure 22 it can be observed that for all the analyzed porosity levels the curves representing the mechanical responses of the UCs with $a < b$ are characterized by a value of the activation stress, i.e. the average stress corresponding to the activation of the
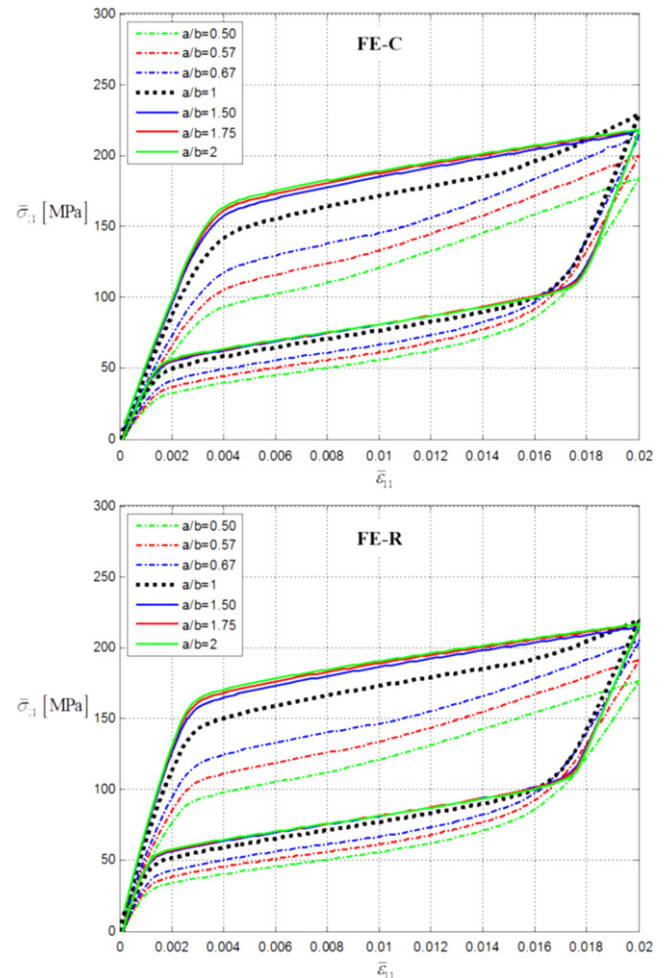
martensite phase transformation, that is lower with respect to the one obtained for the case of a circular pore. Further, the value of the activation stress tends to decrease for decreasing values of the ratio a/b, i.e. for elliptical voids with increasing value of the radius lying on the direction orthogonal to the load application. On the contrary, for the UCs with $a > b$ the activation stress is greater than the one assessed for the UC with a circular pore and the difference tends to increase for increasing values of the ratio a/b. Both these remarks become more evident for higher levels of porosity. Clearly, the value of the overall activation stress depends on the stress intensity factor that occurs around the void.

Also the maximum average stress achieved at the end of loading phase $\left(\bar{\sigma}_{11}^{\,max} \right)$ sensibly varies according to the shape of the pore, especially for high porosity. Notably, it is observed that for a volume fraction of voids equal to 10% the case of a circular pore allows for the maximum value of $\left(\bar{\sigma}_{11}^{\,max} \right)$. Considering elliptical pores the maximum average stress decreases and, specifically, the cases with $a < b$ provide lower values of $\left(\bar{\sigma}_{11}^{\,max} \right)$ compared to the correspondent cases with $a > b$. These outcomes still hold for a
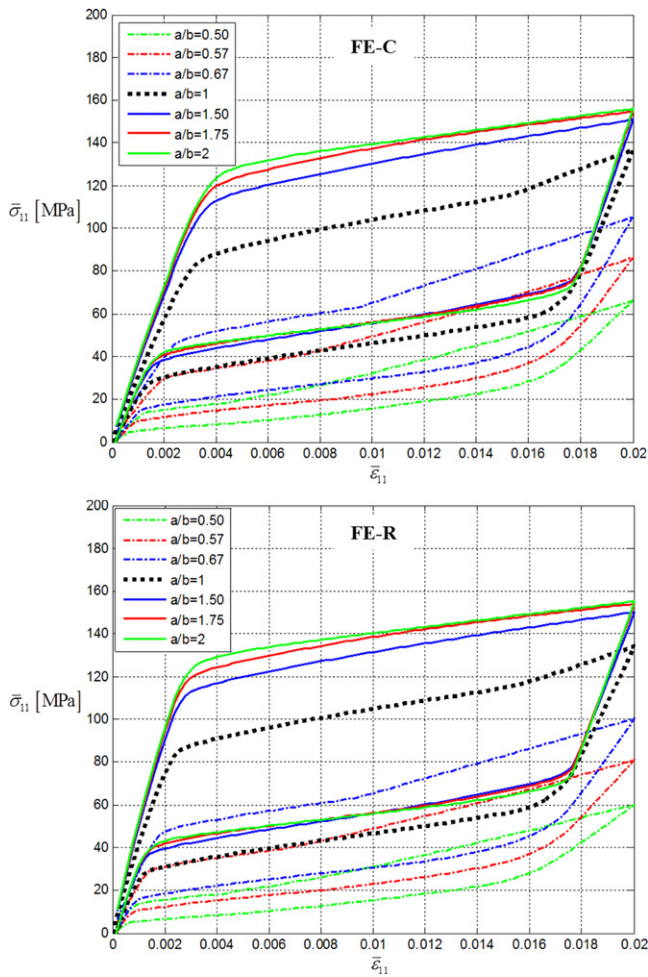
Figure 22. Mechanical responses of the porous UCs with elliptical voids for $f = 0.35$.

Figure 23. Dissipated energy per solid volume for porous NiTi UCs with elliptical pores characterized by different ratios a/b for the analyses: FE-C (a), FE-R (b).

porosity level of 20%. Specifically, for $f = 0.20$ the mechanical responses of the UCs with a/b equal to 1.50, 1.75 and 2 are almost the same, with very close values of the activation stress and of $\left(\bar{\sigma}_{11}^{\ max}\right)$, higher than the corresponding values of the analyses with a/b equal to 0.50, 0.57, 0.67.

For $f = 0.35$ the discrepancies between the activation stress and the maximum stress achieved for the different ratios a/b are more significant. In particular, it can be observed that the curves corresponding to the UCs in which the elliptical voids have the maximum radius lying on the direction of the load application, are characterized by higher values of $\left(\bar{\sigma}_{11}^{\ max}\right)$ with respect to the ones achieved for the case of the circular pore and especially to the ones provided by the UCs with $a < b$.

It can be remarked that the higher the porosity, the more important is the role played by the shape of the void. In particular, for $f = 0.35$ decreasing the ratio a/b the stress concentration increases, thus the transformation occurs for lower value of the average stress, leading to a lower maximum stress.

All these statements result to be true for the all the performed FE-C and FE-R analyses, since adopting the two different expressions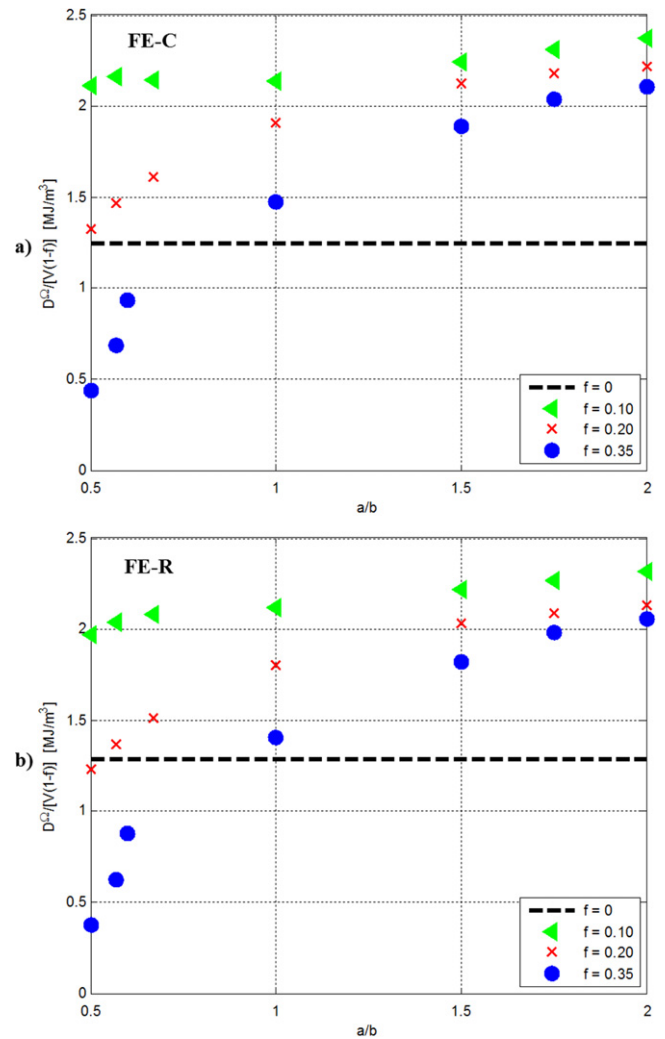 for the elastic constitutive tensor leads to the same qualitative response of the porous SMA. The main differences between the results provided by the two approaches stem in the prediction of the maximum average stresses achieved for $\eta = 0.02$ which are slightly higher for the FE-C analysis, in agreement with the results of the first loading history of the previous numerical test.

It can be also noted that, for a given porosity, the initial stiffness of the UC increases with the ratio a/b, as it could be expected. Moreover, a quite sudden change of slope can be observed in many overall stress–strain curves due to the fulfillment of the martensite transformation in a significant part of the UC.

An interesting issue is also the analysis of the influence of the shape and orientation of voids on the energy absorption capability of the examined porous SMA. Thus, the energy dissipated per volume of the slice of unit thickness of the solid is evaluated in function of the ratio a/b and it is plotted for the FE-C and FE-R analyses in figures 23(a) and (b), respectively. In these figures also the energy dissipated by the dense SMA is reported with dashed lines.

From figure 23 it can be noticed that the porous SMA capacity to dissipate energy is strongly influenced by the shape of the pores and by their orientation with respect to the applied loading. In details, for each value of the volume fraction of voids, the dissipated energy increases with the increasing values of the ratio a/b for all the performed analyses. The increase in the energy dissipation capability is significantly more evident for a high porosity level ($f = 0.35$) and for $a/b < 1.75$, while it is rather limited for the case $f = 0.10$ and for $a/b > 1.75$.

Furthermore, the energy per volume of the slice of unit thickness of the solid dissipated by the porous SMA is always higher than the one dissipated by the dense SMA except for $f = 0.35$ and $a/b < 1.0$.

As established in the previous numerical simulation, also the performed application puts in evidence that value of the dissipated energy depends slightly on the assumption made on the constitutive SMA tensor: the FE-C analyses lead to a slightly higher value of the energy dissipation capability of the porous SMA with respect to the results assessed by the FE-R ones.

5. Conclusions

The micromechanical behavior and the homogenized response of porous SMA is studied in the present work. In particular, nonlinear micromechanical analyses are performed introducing the hypothesis of a periodic distribution of voids, all characterized by the same shape and size; thus, a typical repetitive UC, representative of the heterogeneous porous material and able to account for the properties of the composite medium, is analyzed.

The numerical results show that, once the material parameters are set on the basis of experimental evidences for dense SMA, the proposed micromechanical model is able to reproduce the experimental results of the porous SMA; in particular, a comparison with a porous SMA subjected to uniaxial compression is presented.

Then, numerical investigations are performed for open and closed pore UCs, prescribing the average strain components. This choice is motivated by the future aim to develop a multiscale displacement-based finite element procedure where these micromechanical analyses are implemented at the Gauss point level to obtain the overall constitutive behavior of the porous material. The following points can be remarked.

- The porosity, the shape and orientation of voids significantly influence the mechanical response of porous SMA and its dissipation capability.
- The geometrical change of the void shape from closed to open influences the mechanical response of the porous SMA and the dissipated energy capability: for the same porosity the closed pore UC and the open pore UC tend to have a qualitative similar overall mechanical response with an almost equal $\bar{\sigma}_{11}^{\max}$ but the closed pore UC is able to dissipate more energy.

- From a qualitative point of view, the results obtained for closed pore UCs are very similar to the ones obtained for open pore UCs both in terms of mechanical response and dissipated energy.
- The porous SMA characterized by ellipsoidal/elliptical voids is able to dissipate less energy with respect to the porous SMA with spherical/circular voids when the maximum radius is orthogonal to the load direction.
- Two-dimensional analyses reveal that the porous SMA characterized by elliptical voids is able to dissipate more energy with respect to the porous SMA with circular voids when the maximum radius is oriented in the same direction of the load.
- In almost all the studied cases, the porous SMA is able to dissipate more energy per solid volume with respect to the dense SMA. In particular, it can be pointed out that for the studied cases the maximum dissipated energy is obtained for porosity from 10 to 30% but also for the other studied porosities the dissipated energy is higher than for the dense SMA.
- The quantity of dissipated energy depends on the applied loading histories; in particular, the larger the UC part involved in the phase transformation, the higher the value of the dissipated energy per solid volume. A close dependence between the dissipated energy and the average value of the single variant martensite has been demonstrated: it is found that the dissipation per solid volume and the average of single variant martensite volume fraction per solid volume show the same trend with respect to the change in porosity.
- The SMA model which considers the same elastic properties for austenite and martensite leads to overall mechanical responses very close to the ones considering different moduli, and for high values of prescribed average strain and porosity it can provide slightly higher values of the dissipated energy.
- For the porous SMA the differences between the FE-C, FE-R and FE-V analyses are less significant than for the dense SMA.

Finally, the performed micromechanical analyses can be very useful for the design of specific devices whose main task is the energy dissipation. In particular, these types of micromechanical analyses allows us to identify from the mechanical properties of the dense SMA the most appropriate porous SMA, in terms of porosity density, shape and orientation, in manufacturing the device.

Acknowledgments

References

[1] Martynova I, Skorohod V, Solonin S and Goncharuk S 1991 Shape memory and superelasticity behaviour of porous Ti–Ni material *J. Physique IV01* **C4** 421–6

[2] Li B-Y, Rong L-J and Li Y-Y 1998 Porous NiTi alloy prepared from elemental powder sintering *J. Mater. Res.* **13** 2847–51

[3] Vandygriff E L, Lagoudas D C, Thangaraj K and Chen Y-C 2000 Porous shape memory alloys *Adaptive Structures and Materials Systems* ed J Redmond pp 64–7

[4] Shabalovskaya S A 1996 On the nature of the biocompatibility and on medical applications of NiTi shape memory and superelastic alloys *BioMed. Mater. Eng.* **6** 267–89

[5] Bansiddhi A, Sargeant T D, Stupp S I and Dunand D C 2008 Porous NiTi for bone implants: a review *Acta Biomater.* **4** 773–82

[6] Xiong J Y, Li Y C, Wang X J, Hodgson P D and Wen C E 2008 Titanium–nickel shape memory alloy foams for bone tissue engineering *J. Mech. Behav. Biomed. Mater.* **1** 269–73

[7] Wen C E, Xiong J Y, Li Y C and Hodgson P D 2010 Porous shape memory alloy scaffolds for biomedical applications: a review *Phys. Scr.* **T139** 1–8

[8] Zhao Y, Taya M and Izui H 2006 Study on energy absorbing composite structure made of concentric NiTi spring and porous NiTi *Int. J. Solids Struct.* **43** 2497–512

[9] Ashrafi M J, Arghavani J, Naghdabadi R and Sohrabpour S 2015 A 3D constitutive model for pressure-dependent phase transformation of porous shape memory alloys *J. Mech. Behav. Biomed.* **42** 292–310

[10] Ashrafi M J, Arghavani J, Naghdabadi R and Auricchio F 2015 A three-dimensional phenomenological constitutive model for porous shape memory alloys including plasticity effects *J. Intell. Mater. Syst. Struct.* doi:10.1177/1045389X15575085

[11] Qidwai M A, Entchev P B, Lagoudas D C and DeGiorgi V G 2001 Modeling of the thermomechanical behavior of porous shape memory alloys *Int. J. Solids Struct.* **38** 8653–71

[12] Entchev P B and Lagoudas D C 2002 Modeling porous shape memory alloys using micromechanical averaging techniques *Mech. Mater.* **34** 1–24

[13] Entchev P B and Lagoudas D C 2004 Modeling of transformation-induced plasticity and its effect on the behavior of porous shape memory alloys: II. Porous SMA response *Mech. Mater.* **36** 893–913

[14] Zhao Y and Taya M 2007 Analytical modeling for stress–strain curve of a porous NiTi *J. Appl. Mech.* **74** 291–7

[15] Zhu Y and Dui G 2011 A model considering hydrostatic stress of porous NiTi shape memory alloys *Acta Mech. Solida Sin.* **24** 289–98

[16] Nemat-Nasser S, Su Y, Guo W G and Isaacs J 2005 Experimental characterization and micro-mechanical modeling of superelastic response of a porous NiTi shape-memory alloy *J. Mech. Phys. Solids* **53** 2320–46

[17] Qidwai M A and De Giorgi V G 2002 A computational mesoscale evaluation of material characteristics of porous shape memory alloys *Smart Mater. Struct.* **11** 435–43

[18] Qidwai M A and De Giorgi V G 2004 Numerical assessment of the dynamic behavior of hybrid shape memory alloy composite *Smart Mater. Struct.* **13** 134–45

[19] Panico M and Brinson L C 2008 Computational modeling of porous shape memory alloys *Int. J. Solids Struct.* **45** 5613–26

[20] Liu B, Dui G and Zhu Y 2012 On phase transformation behavior of porous shape memory alloys *J. Mech. Behav. Biomed. Mater.* **5** 9–15

[21] Sepe V, Marfia S and Auricchio F 2014 Response of porous SMA: a micromechanical study *Frattura ed Integrità Strutturale* **29** 85–96

[22] Souza A C, Mamiya E N and Zouain N 1998 Three-dimensional model for solids undergoing stress-induced phase transformations *Eur. J. Mech.* A **17** 789–806

[23] Auricchio F and Petrini L 2004 A three-dimensional model describing stress-temperature induced solid phase transformations: solution algorithm and boundary value problems *Int. J. Numer. Methods Eng.* **61** 807–36

[24] Evangelista V, Marfia S and Sacco E 2009 Phenomenological 3D and 1D consistent models for shape memory alloy materials *Comput. Mech.* **44** 405–21

[25] Auricchio F and Sacco E 1997 A one-dimensional model for superelastic shape-memory alloys with different elastic properties between austenite and martensite *Int. J. Non-Linear Mech.* **32-6** 1101–14

[26] Zienkiewicz O C and Taylor R L 1991 *The Finite Element Method* 4th edn (London: McGraw-Hill)

[27] Suquet P 1987 Elements of homogenization for inelastic solid mechanics *Homogenization Techniques for Composite Media* (*Lecture Notes in Physics* vol 272) ed E Sanchez-Palencia and A Zaoui (Berlin: Springer) pp 194–275

[28] Luciano R and Sacco E 1998 Variational methods for the homogenization of periodic heterogeneous media *Eur. J. Mech.* A **17-4** 599–617

[29] Arghavani J, Auricchio F, Naghdabadi R, Reali A and Sohrabpour S 2010 A 3D phenomenological constitutive model for shape memory alloys under multiaxial loadings *Int. J. Plast.* **26** 976–91

[30] Saleeb A F, Padula S A and Kumar A 2011 A multi-axial, multimechanism based constitutive model for the comprehensive representation of the evolutionary response of SMAs under general thermomechanical loading conditions *Int. J. Plast.* **27** 655–87

[31] Gu X, Zaki W, Morin C, Moumni Z and Zhang W 2015 Time integration and assessment of a model for shape memory alloys considering multiaxial nonproportional loading cases *Int. J. Solids Struct.* **54** 28–9

[32] Lecce L and Concilio A (ed) 2015 *Shape Memory Alloy Engineering: For Aerospace, Structural and Biomedical Applications* (Boston: Butterworth-Heinemann)

[33] Lemaitre J and Chaboche J 1988 *Mecanique des Materiaux Solides* (Paris: Dunod)

[34] Zhao Y, Taya M, Kang Y S and Kawasaki A 2005 Compression behavior of porous NiTi shape memory alloy *Acta Mater.* **53** 337–43

[35] Greiner C, Oppenheimer S M and Dunand D C 2005 High strength, low stiffness, porous NiTi with superelastic properties *Acta Biomater.* **1** 705–16

[36] Imwinkelried T 2007 Mechanical properties of open-pore titanium foam *J. Biomed. Mater. Res.* A **81** 964–70

[37] Wang X, Li Y *et al* 2009 Porous TiNbZr alloy scaffolds for biomedical applications *Acta Biomater.* **5** 3616–24